12-2012

Modeling Lithospheric Rheology from Modern Measurements of Bonneville Shoreline Deformation

Eric P. Beard

MODELING LITHOSPHERIC RHEOLOGY FROM MODERN MEASUREMENTS OF BONNEVILLE SHORELINE DEFORMATION

by

Eric P. Beard

A thesis submitted in partial fulfillment
of the requirements for the degree

of

MASTER OF SCIENCE

in

Geology

Approved:

Anthony R. Lowry, Ph.D. Major Professor	W. Adolph Yonkee, Ph.D. Committee Member
Joel L. Pederson, Ph.D. Committee Member	Mark R. McLellan, Ph.D. Vice President for Research and Dean of the School of Graduate Studies

UTAH STATE UNIVERSITY
Logan, Utah

2012

ABSTRACT

Modeling Lithospheric Rheology from Modern Measurements of Bonneville Uplift

by

Eric P. Beard, Master of Science

Utah State University, 2012

Major Professor: Anthony R. Lowry
Department: Geology

Here I develop a cross-correlation approach to estimating heights of shoreline features, and apply the new method to paleo-shorelines of Pleistocene Lake Bonneville. I calculate 1st-derivative (slope) and 2nd-derivative (curvature) profiles from Digital Elevation Model (DEM) or Global Positioning System Real-Time Kinematic (GPS-RTK) measurements of elevation. I then cross-correlate pairs of profiles that have been shifted by various "lags," or shifts in elevation. The correlation coefficient (a normalized dot-product measure of similarity) is calculated as a function of lag within small (~40 m) windows centered at various elevations. The elevation and lag with the greatest correlation coefficient indicates the shoreline elevation at the reference profile and the change in shoreline height for the profile pair. I evaluate several different algorithms for deriving slope and curvature by examining closure of elevation lags across profile triples.

I then model isostatic response to Lake Bonneville loading and unloading. I first model lakeshore uplift response to lake load removal assuming an elastic layer

over an inviscid half-space. I obtain a best-fit comparison of predicted to observed shoreline heights for the Bonneville level with an elastic layer thickness, T_e, of 25±2 km (at 95% confidence) when using only previously published shoreline elevation estimates. The best-fit for the Bonneville level when using these estimates plus 44 new estimates suggests a T_e of 26±2 km. The best-fit model for the Provo level suggests T_e of 17±3 km. For the Gilbert level, the response is insensitive to the assumed T_e. I next model isostatic response to Bonneville loading and unloading assuming an elastic layer over a viscoelastic halfspace. This approach assumes constant parameters for the entire loading history, and yields a best-fit model with T_e =70±5 km and viscosity η=~2x10^{18} Pa s with 95% confidence ranging from ~1x10^{18} to ~5x10^{19} Pa s when only the previously published data are used. With the newer data added, the best-fit model has T_e =58±2 km and η ranging from ~1x10^{18} to ~1x10^{19} Pa s with 95% confidence. The 12-15 m weighted root-mean-square misfit to the best-fitting model is dominated by tectonic signals related to Basin-and-Range tectonics particularly seismic offsets of the Wasatch fault, and closely mimics the geological timescale pattern of basin-subsidence and range-uplift.

(91 Pages)

PUBLIC ABSTRACT

Modeling Lithospheric Rheology from Modern Measurements of Bonneville Uplift

by

Eric P. Beard, Master of Science

Utah State University, 2012

Major Professor: Anthony R. Lowry
Department: Geology

Here I develop a new method for estimating differences in elevation between pairs of paleo-lake shoreline features. This method is applied to Lake Bonneville, a large lake that inundated nearly 1/3 of the state of Utah as well as parts of Nevada and Idaho from 34 to 11.5 thousand years ago. Under the weight of the lake water load, the surface of the Earth was depressed by up to 75 m. This occurred as Earth mantle rock at depth flowed outward in response to the weight of the lake. I use this new methodology to compile here a denser sample of Lake Bonneville shoreline elevations. The denser data are then used to develop a new model of how the Earth flows at depth in response to a load such as Lake Bonneville. Because rock flow also drives earthquakes, this has the potential to improve assessments of earthquake hazard in the region. With more than one million people currently residing within the corridor of strong ground motion for future earthquake events on the Wasatch

Fault, the most active fault in the region, this has the potential to reduce damage to structures and risk to life and property of Wasatch Front residents.

ACKNOWLEDGMENTS

This thesis was funded by the National Science Foundation, grant # EAR-0955909 awarded to Dr. Anthony R. Lowry. Field research was funded by a generous donation from the Rocky Mountain Association of Geologists. Topographic maps and Digital Elevation Models used in this study were provided by the Utah Automated Geographic Reference Center and the United States Geological Survey.

I would like to thank my thesis advisor, Dr. Anthony R. Lowry, for all of his patience in helping me understand the quantitative aspect of this research and helping me develop a passion for the mathematics that describes the universe around us. He was always very kind even when I could tell he had to bite his tongue to keep from reprimanding me after asking him to explain the same mathematical concepts time after time. I would also like to thank my committee members, Drs. Joel L. Pederson and W. Adolph Yonkee, for their time and mentorship as I progressed through the process of developing my research.

Special thanks to Dr. Bruce G. Bills for taking the time to help me acquire and understand much of the data that I used in this projects, and also to Dr. Charles "Jack" Oviatt for spending a hot summer day explaining the geomorphology of Lake Bonneville in the field.

I need to thank my undergraduate assistants, J.R. Hoggan and Matt Rahmeyer, who endured some difficult days in the field hiking up some extremely steep terrain in order to help me collect valuable data.

Last, but definitely not least, my heartfelt thanks goes out to my wife, Patsy, for her incredible patience, forgiveness, and love that she has shown me during this

difficult time, and to my children for patiently sacrificing time with their father as I pursued my dream. Thank you all for your help and support.

Eric Beard

CONTENTS

Page

ABSTRACT....iii

PUBLIC ABSTRACT....v

ACKNOWLEDGMENTS....vii

LIST OF FIGURES....xi

CHAPTER

1 INTRODUCTION....1

References....3

2 CROSS-CORRELATION MEASUREMENTS OF HEIGHT VARIATIONS OF GEOMORPHIC FEATURES....4

Abstract....4
Introduction....4

History of Lake Bonneville....4
Previous Work on Shorelines....7

Methods....11

Data Collection....11
Data Analysis....14
Synthetic Testing....16
Testing Real Data....21
Modifications to Optimize the Method....26

Weighted Least Squares Inversion....26
Bootstrap Re-weighting....28
Wiener Filtering....32

Methodological Comparison....31

Discussion....38
References....39

3 MODELING ISOSTATIC RESPONSE WITH NEW ESTIMATES OF BONNEVILLE SHORELINE ELEVATIONS....42

Abstract....42
Introduction....43
Isostatic Modeling....48

Elastic-Over-Inviscid Modeling of Currey Data Only....49
Augmentation of the Currey (1982) Data....52
Elastic-Over-Inviscid Modeling of Augmented Data....56
Elastic-Over-Viscoelastic Model....59

Discussion....64
Conclusions....66
References....67

4 SUMMARY AND DISCUSSION OF IMPLICATIONS....70

Summary of Results....70
Implications of T_e Results....71
References....74

APPENDIX....76

LIST OF FIGURES

Figure		Page
2.1	Lake depths for the Bonneville, Provo, and Gilbert stages	6
2.2	Shoreline Profile	8
2.3	Gilbert's (1890) contour map of Bonneville uplift	10
2.4	Idealized profiles of a shoreline and its derivatives (from Hare et al., 2001)	14
2.5	Synthetic shoreline profiles	17
2.6	1st derivative (slope) of synthetic profiles	18
2.7	2nd derivative (curvature) or synthetic profiles	19
2.8	1st and 2nd derivative correlograms for synthetic profiles	21
2.9	Shoreline profile from 2-m auto-correlated DEMs near Lakeside, Utah	22
2.10	1st derivative (slope) of profiles in figure 2.9	22
2.11	2nd derivative (curvature) of profiles in figure 2.9	23
2.12	1st and 2nd derivative correlograms for profiles in figure 2.9	23
2.13	1st and 2nd derivative contour plots for profiles in figure 2.9	24
2.14	Stacked contour plots and confidence intervals for profiles in figure 2.9	26
2.15	Stacked contour plots and confidence intervals for WLS inversion of slope for profiles in figure 2.9	28
2.16	1st derivative (slope) of profiles taken from 5-m auto-correlated DEMs in Cache Valley, Utah	29
2.17	2nd derivative (curvature) of profiles in figure 2.16	30
2.18	Comparison of slope and curvature with bootstrap re-weighting	31

2.19 Profile locations used for testing the algorithm....34

2.20 Comparison of weighted means of lag and uncertainties for three approaches compared to lag of outlier approach....36

2.21 Comparison of weighted means of lag and uncertainties from 2-m and 5-m resolution data....37

2.22 Comparison of shoreline elevations and uncertainties from 2-m and 5-m resolution data....38

3.1 Lake depths for the Bonneville, Provo, and Gilbert stages....44

3.2 Modeled and observed isostatic response for Bonneville epoch....49

3.3 Misfits of observed and modeled response at various T_e....50

3.4 Residual map of modeled vs. observed response for Bonneville stage....51

3.5 Location of shoreline estimates....53

3.6 Profile of barrier ridge on Antelope Island, Utah....54

3.7 Elevation and curvature profile of erosional shoreline on Antelope Island, Utah....55

3.8 Comparison of modeled vs. observed response misfits for Currey's (1982) observations and the augmented dataset....56

3.9 Comparison of modeled response to observed response from Currey's (1982) observations and from the augmented dataset, Bonneville stage....57

3.10 Residual maps of modeled vs. observed responses from Currey's (1982) observations and from the enhanced dataset, Bonneville stage....58

3.11 RMS misfit of T_e and viscosity pairs from viscoelastic modeling....61

3.12 Point map of Bonneville sampling locations for observed and modeled response....62

3.13 Point map of Provo level sampling locations for observed and modeled response....63

3.14 Modeled suppression of fault activity due to Bonneville loading (from Hetzel and Hampel, 2005).....65

4.1 Yield-strength envelopes (from Burov and Diament, 1995).....72

CHAPTER 1

INTRODUCTION

The Great Salt Lake in northern Utah is all that remains of Lake Bonneville, a large lake that existed during the last glacial period, with a maximum surface area of around 52,000 km^2 and depths in excess of 300 m. The lithosphere was depressed as hot rock deep within the earth flowed outward in response to the tremendous load exerted by the lake water. After the load was removed, the lithosphere returned more or less to its original position, leaving shorelines that are as much as 75 m higher in elevation at the center of the basin than around the periphery (Currey, 1982). G.K. Gilbert observed this phenomenon and developed multiple hypotheses to explain this observation (Gilbert, 1890). One hypothesis posited that the differential heights of shorelines could represent deformation of a rigid plate over a fluid substrate. This thesis reaffirms Gilbert's original hypothesis by modeling lakeshore height observations as the isostatic response of an elastic plate over a fluid substrate using loads estimated from the shoreline elevations.

The thesis also describes a methodology for measuring variations in shoreline elevation, applied directly to Pleistocene Lake Bonneville. Using this method, I extract shoreline elevation data for the Bonneville stage of the lake's history from the footwall of the Wasatch Fault and several other key locations in the basin. These new data are used to examine possible inaccuracies due to sampling biases inherent in the most recent and complete prior shoreline elevation dataset, compiled by Currey (1982). The potential for bias is examined by comparing

models of the isostatic response of the lithosphere to lake unloading derived from the Currey (1982) data alone versus those using the enhanced dataset.

Since Gilbert, many researchers have undertaken studies of Lake Bonneville, both to understand the past climate of the basin and to quantify the dynamical flow processes responsible for isostatic rebound and other Earth deformation. Currey's (1982) monumental effor compiled 181 shoreline elevation estimates for the Bonneville level of the lake (~17.8-17.4 ka), 112 for the Provo level of the lake (~17.4-15.2 ka), and 43 for the Gilbert level of the lake (~12.5-11.5 ka). This was accomplished without the benefit of computational mapping tools, and the data were rudimentary by today's standards. There are also sampling biases inherent in the data. Currey (1982) took nearly all of his estimates from depositional shoreline features, resulting in relatively few estimates on the footwall of the most active fault in the region, the Wasatch Fault. Coseismic deformation during earthquakes is a large signal superposed on the isostatic signal modeled in rebound studies, so preferential sampling of the Wasatch hanging wall biases measurements there toward anomalous subsidence along the Wasatch Front. Moreover, coseismic offset of the Wasatch since Bonneville highstand is a desirable piece of information from a seismic hazard perspective.

In Chapter 2 I develop an algorithm to estimate differences in elevation between pairs of erosional shorelines, using cross-correlation and stacking of topographic slope and curvature from densely-sampled Digital Elevation Models (DEMs). These data are used to examine potential effects of sampling bias in the

widely-used Currey (1982) dataset and evaluate the impact of more complete sampling on models of isostatic response to Bonneville unloading.

The goal is to develop a quantitative approach to estimating heights of geomorphic features from modern DEMs that others in the scientific community will find useful. In addition to quantifying shoreline elevations, it may be useful for other applications such as quantifying differences in surface offset of fault scarps. This method may enable researchers to estimate the differences in scarp offset with greatly reduced cost, labor and environmental impact relative to trenching.

A more immediate application of this algorithm will be to enhance Lake Bonneville shoreline datasets used to model rheology. Better understanding the rheology beneath the Bonneville Basin, a seismically active region, will enable improved modeling of the evolution of stress and strain associated with faulting and a more predictive model of the seismic hazard for the region. Towards this end, in Chapter 3, I develop some simple models that examine the effects of sampling bias and the importance of accurate measurements, such as the shoreline picking algorithm can provide, toward developing an optimal model of rheology.

References

Currey, D.R., Lake Bonneville: Selected features of relevance to neotectonic analysis, *U.S. Geol. Surv. Open File Rep., 82-1070*, 31 pp., 1982.

Gilbert, G.K., Lake Bonneville, *U.S. Geol. Surv. Monogr., 1*, 438 pp., 1890.

CHAPTER 2

CROSS-CORRELATION MEASUREMENT OF HEIGHT VARIATIONS OF GEOMORPHIC FEATURES

Abstract

This chapter describes a cross-correlation approach to identify elevation "lags" in shoreline topographic breaks. The method is applied to paleo-shorelines of Lake Bonneville. 1st-derivative (slope) and 2nd-derivative (curvature) profiles of elevation are calculated from Digital Elevation Model (DEM) or Global Positioning System Real-Time Kinematic (GPS-RTK) measurements of elevation. Pairs of profiles are then cross-correlated within ~40 m windows that are shifted by various "lags", or shifts in elevation. The correlation coefficient (a normalized dot-product measuring similarity) is calculated as a function of lag and elevation of the window center. The elevation and lag with the greatest correlation coefficient indicates the shoreline elevation at the reference profile and the difference in shoreline height for the profile pair. I evaluate several different algorithms for calculating slope and curvature by examining closure of elevation lags across profile triples.

Introduction

History of Lake Bonneville

During the last glacial maximum, many basins in the Basin and Range Province were filled by pluvial lakes as late Wisconsinan glacial conditions increased effective moisture by as much as 33% (Lemons et al., 1996). The largest

of these was Lake Bonneville, with a surface area of ~52,000 km^2 at high-stand and a maximum depth in excess of 350m (Bills et al., 1994). Lake level history originally interpreted by Currey (1990) has been corrected to calendar dates following calibration of the ^{14}C timescale (Bard et al., 1990) and otherwise improved by additional sampling of the Bonneville epochs (Godsey et al., 2005, 2011; Nishizawa, 2010). Recently published research infers that the lake began rising from roughly its current level around 34 ka and progressed through a quasi-linear step-wise transgression until it reached its maximum level (the Bonneville) ~17.8 ka (Currey, 1990; Godsey et al., 2005, 2011). An outlet near Zenda, Idaho controlled the Bonneville high-stand (Gilbert, 1890; Currey, 1982, 1990; Janecke and Oaks, 2011). After occupying this level for around 400 years, the interlocking alluvial fans damming the lake near Zenda failed catastrophically and the lake level dropped by more than 100 m over a short (<100 yr) interval (O'Connor, 1993; Oviatt, C.G., personal communication, 2011). Bedrock with greater integrity near Swan Lake, Idaho controlled the subsequent Provo threshold (Janecke and Oaks, 2011). The lake occupied the Upper Provo level for ~1500 years from ~17.4-15.9 ka (Godsey et al., 2011). Following a brief and possibly sudden decrease in level, the lake re-equilibrated at a Lower Provo level about 10 m below the upper soon after 15.9 ka (Godsey et al., 2005; Janecke and Oaks, 2011). The lake remained at this level until roughly 15.2 ka (Benson et al., 2011). As climate warmed and precipitation decreased, the lake regressed to roughly its current level by about 13.5 ka (Currey, 1990; Godsey et al., 2011). There was a brief transgression to the Gilbert level around 12.5 ka, which lasted less than 1000 years (Benson et al., 2011). Estimates

of lake depth and extent for the Bonneville, Provo and Gilbert stages are shown in Figure 2.1.

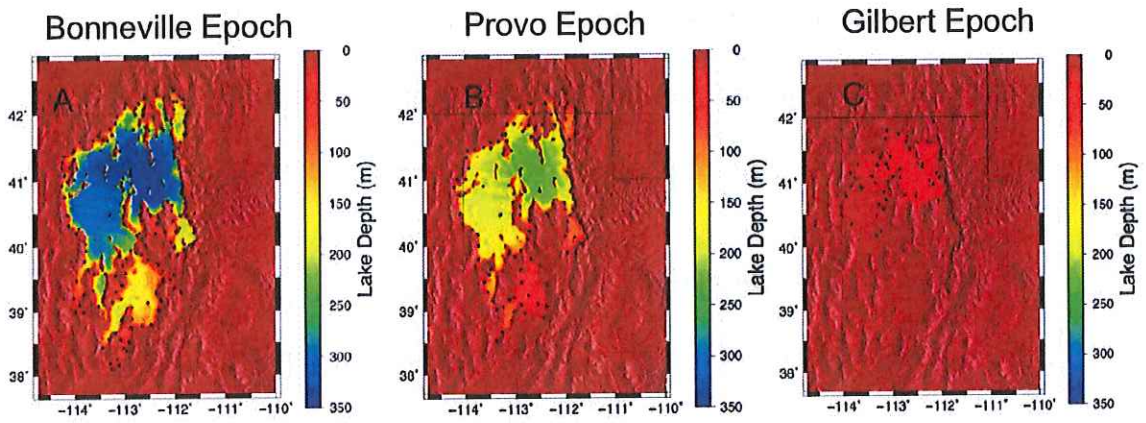

Figure 2.1: Lake depths during the three main levels of Lake Bonneville, estimated by subtracting modern topography from paleoshoreline elevation data points (Currey, 1982). (A) Bonneville epoch (~17.8-17.4 ka); (B) Provo epoch (~17.4-15.2 ka); (C) the Gilbert epoch (~12.5-11.5 ka).

Nishizawa (2010) interpreted an alternative history based on stratigraphy, sedimentology, geomorphology, radiocarbon dating, and tephra identification differs significantly from the chronology presented above. Most significantly, he argues that the lake grew to exceed the Provo threshold during multiple events, the most recent of which post-dates the Gilbert occupation and persisted for over 1000 years until around 10.3 ka. However, although opinions differ on lake level history, the lake level history described above (sans modification by Nishizawa (2010)) is more broadly accepted and thus is used in this thesis for modeling lake load history.

The remnant shorelines of Lake Bonneville provide a useful laboratory for research into paleoclimatology and rheology of the lower crust and upper mantle. Shorelines elevations vary across the Bonneville basin as first observed by Gilbert (1890), indicating dynamical flow isostatically adjusted for the changes in lake mass.

Lake Bonneville shorelines are well-preserved and strongly constrain the depth and lateral extent of the lake load. Moreover, the history of lake transgression and regression is well-sampled by modern dating techniques. The combination of spatial and temporal sampling of lake loading and shoreline deformation promises great potential for estimation of poorly-known parameters of ductile flow rheology.

Previous Work on Shorelines

An accurate dataset of shoreline elevation measurements is needed before the isostatic response can be modeled. The shorelines fall into two broad process categories: depositional and erosional. Gilbert (1890) identified depositional shorelines as features including barriers, tombolos and spits that are constructed from sediment deposited primarily by longshore transport. Erosional shorelines primarily occur as wave-cut straths and are prominent where the shoreline is located in areas of greater relief, such as along the Wasatch Fault (Gilbert, 1890).

Historically, depositional shorelines have been the primary source of shoreline elevation estimates because a paleolake elevation can be estimated at the crest of the feature (Currey, 1982). The relationship of depositional shoreline features to mean paleolake levels is complicated by the fact that they can be super-elevated, coincident, or sub-elevated. However, the relationship of the crest to lake level can be discerned observationally (Currey, 1982).

The point of maximum curvature (or knickpoint) of an erosional shoreline represents the furthest extent of backwash from wave activity and has been identified as the maximum lake level (Hare et al., 2001; Oviatt, 2011). Colluvial

wedges often obscure the original knickpoint of an erosional shoreline, which has the dual effect of biasing toward a lower estimate of knickpoint height and impeding visual identification of the knickpoint. For a shoreline in equilibrium, the knickpoint will be slightly higher than the mean water level because it represents the maximum height of backwash from waves, particularly during storm activity (Fig. 2.2). The height difference between knickpoint and lake level has a complicated dependence on local wave dynamics, erosional resistance of the substrate, and maturity of the shoreline (Oviatt, 2011).

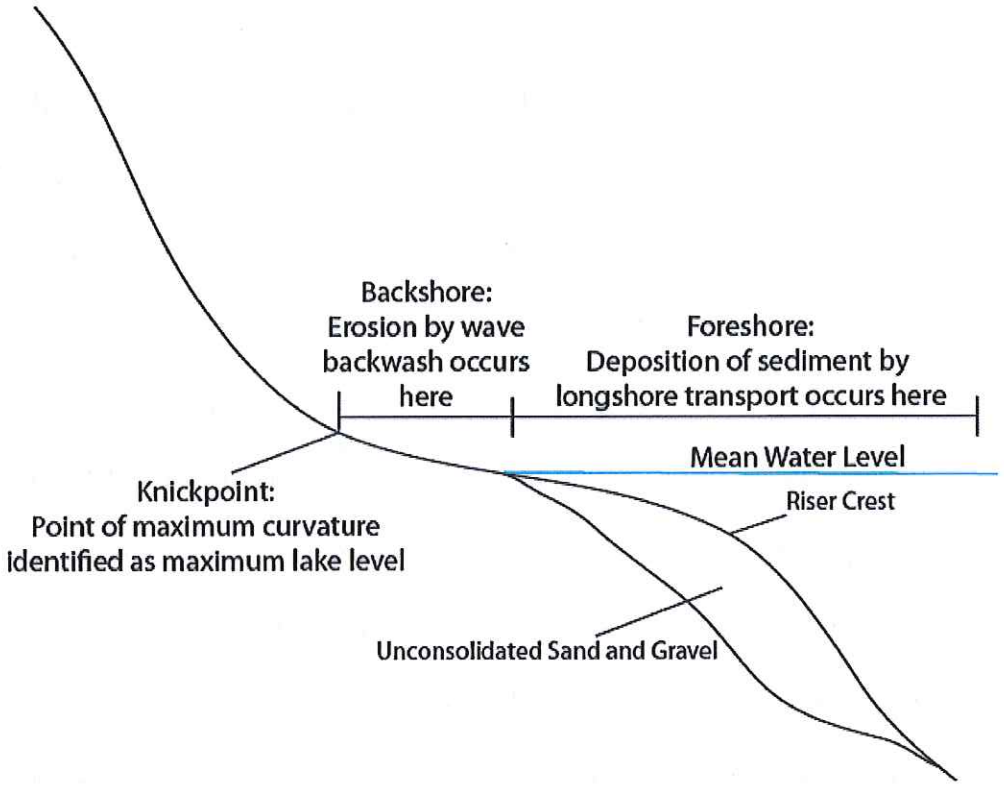

Figure 2.2: A simple shoreline profile depicting the location of the knickpoint in relation to the mean water level for an erosional shoreline in equilibrium. The backshore is the zone of backwash from waves and the zone of erosion. Its size is controlled by storm activity. The riser crest is the maximum extent of the benchtop into the lake and its location is controlled by the amount of sediment accumulation and the angle of repose on the riser inflection below.

Field observations confirm the complicated nature of the relationship between lake level and feature height. Near Grouse Creek, Utah, a depositional shoreline intersects an erosional shoreline of the same age and appears to be slightly higher than the erosional shoreline. However, an erosional shoreline on Antelope Island, Utah, has a very clear knickpoint signal that is about 3 m higher than the highest point on a depositional shoreline that is only 250 m away. Possible explainations for the differences at these two locations include the maturity of the erosional shorelines and the elevations of the depositional shorelines relative to lake level. Distinguishing between these possibilities would require much more laborious observation of the features than I have performed for this thesis, but it is worth bearing in mind that errors of up to several meters are introduced by treating feature elevation as a direct proxy for lake level. I will examine the importance of this proxy error relative to other sources of measurement later in this chapter. Gilbert (1890) compiled the first shoreline elevation dataset for Lake Bonneville by measuring 30 point-elevations for the Bonneville epoch and 10 for the Provo epoch using spirit levels transported by horse and mule. His contour map of shoreline elevations for the Bonneville level (Figure 2.3) illustrates a picture of isostatic uplift following removal of the lake load that has changed only incrementally with subsequent improvements in sample density and measurement technology. Crittenden (1963) compiled a shoreline elevation dataset with 39 shoreline elevations taken from previous researchers, including Gilbert (1890), and an additional 51 original shoreline elevation measurements "...made almost entirely by

photogeologic methods" (Crittenden, 1963). These 90 shoreline measurements were all for the Bonneville level.

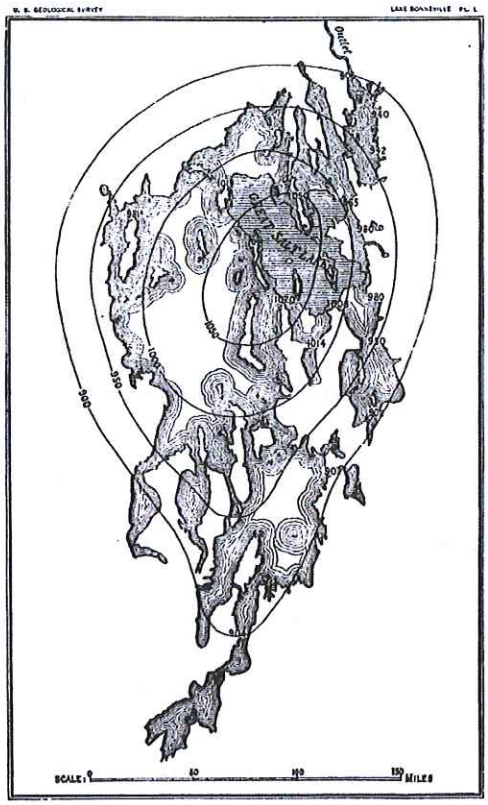

Figure 2.3: Gilbert's (1890) diagram illustrating contours of shoreline height variations evident on Bonneville shorelines.

Currey (1982) compiled the most comprehensive Lake Bonneville shoreline elevation dataset to-date. The dataset is composed almost entirely of depositional shoreline elevations due to the relative simplicity of measuring depositional crests from aerial photos. Care was taken to avoid assigning elevations to strongly developed depositional shoreline ridge features that were likely super-elevated, focusing instead on more weakly developed landforms that were more likely to be coincident with mean surface elevation (Currey, 1982). Currey (1982) did not correct for super- or sub-elevation of features, deeming it "improbable" that such

corrections would exceed the 1 to 4 m uncertainties he estimated for interpolation of topographic map contour intervals to feature locations.

Though less common than erosional shorelines, depositional shorelines occur throughout the basin, and Currey's (1982) dataset appears to sample the entire lake at a more-or-less uniform spacing. However, very few of these points are on the footwall of the Wasatch Fault, the most active fault in the region. Coseismic deformation during earthquakes is likely to be the largest source of error in modeling isostatic response to lake unloading, and is largest near the normal fault with up to several meters of hanging-wall subsidence and smaller amounts of footwall uplift (Barrientos et al., 1987). Most estimates near the Wasatch are on the hanging-wall, and the few elevation estimates on the Wasatch footwall are far from the fault trace where coseismic tectonic uplift is minimal. Consequently Wasatch Fault coseismic deformation may substantially bias models of isostatic response. Erosional Bonneville shorelines are plentiful on the Wasatch footwall so a method for accurately extracting erosional shoreline elevations might yield a more complete, less biased sample of lake level.

Methods

Data Collection

Elevation data for this study derive from: (1) field measurements collected with Global Positioning System instruments in Real-Time Kinematic positioning mode (GPS-RTK), and (2) Digital Elevation Models (DEMs) available from the Utah state Geographic Information Systems (GIS) data clearing house (AGRC, 2010).

DEMs derive from two different types of raw data products, with correspondingly different quality. Five-meter-resolution "auto-correlated" DEMs, derived from a stereoscopic correlation analysis of circa 2006 aerial photos, are available for the entire state of Utah. Two-meter-resolution DEMs also developed from aerial photos through auto-correlation techniques are available for a small portion of the basin, mainly near highly populated areas along the Wasatch Front. Two-meter-resolution LiDAR data, flown as part of the EarthScope-LiDAR program for the Open Topography Portal, is available for an even smaller part of the basin, focused immediately on the urban population centers along the Wasatch Front from North Ogden, Utah in the north to Draper, Utah in the south. In each case, these terrain (*x, y, z*) models have units of m easting and northing in a NAD83 datum with elevation *z*-values in NAD88.

GPS-RTK surveys of shoreline profiles were conducted at six locations specifically for this study, with the support of funding from the Rocky Mountain Association of Geologists (RMAG). Only one of these locations yielded accurately referenced elevation data from which a shoreline elevation can be measured. The others were nevertheless used to develop the algorithm described below and were instrumental in the success of this research effort. The RTK systems available for this study are accurate to within a few centimeters in elevation. At most locations, multiple, parallel surveys running roughly orthogonal to the shoreline trace were collected, spaced about 5 m apart in a swath 25-50 m wide, from which an averaged elevation profile can be derived. The averaging, or "stacking," of elevation measurements reduces effects of some noise sources including instrument error,

operator positioning of the antenna, erosional rills and boulders. It also permits calculation of a variance for each elevation measurement along the profile to facilitate a more robust statistical analysis.

From the DEMs, I extracted an analogous 25-50 m wide swath of data roughly orthogonal to the azimuth of the shoreline. For both the GPS-RTK and DEM data, a small swath of DEM data are extracted parallel to the shoreline trace near the profile location to help define transformation parameters for rotating *x-y* positions into a shoreline-perpendicular frame.

Shoreline preservation is key to accurate measurement, and thus I looked for locations with minimal disruption by erosional rills and colluvial wedges accumulation. When possible, I physically visited the shoreline. In all cases, a combination of Google Earth (Google®, 2011) and the Arc GIS suite (ESRI®, 2010) were used to identify shorelines with minimal perturbation by stream channels, talus slopes, and swales. The method described here also requires a minimum of 25 to 50 m width of well-preserved feature and at least 60-70 meters of relief above and below the shoreline. Optimal locations for data extraction included exceptionally wide and tall triangular facets on the footwall of a normal fault. However, it was often difficult to find a shoreline meeting all of these criteria. Consequently in a few instances I extracted elevation data that included a talus slope above the shoreline.

Data Analysis

Hare et al. (2001) previously developed a slope and curvature analysis of topographic features in an erosional shoreline profile. They not that the lake-ward maximum in first-derivative (slope) is expected to correspond to a riser inflection and the minimum slope to the "benchtop" of the terrace (Figure 2.4). The minimum in the second-derivative (curvature) of the profile is expected at the riser crest, the point of break in slope from the riser inflection to the benchtop. The point of maximum curvature should be at the knick-point (Figure 2.4).

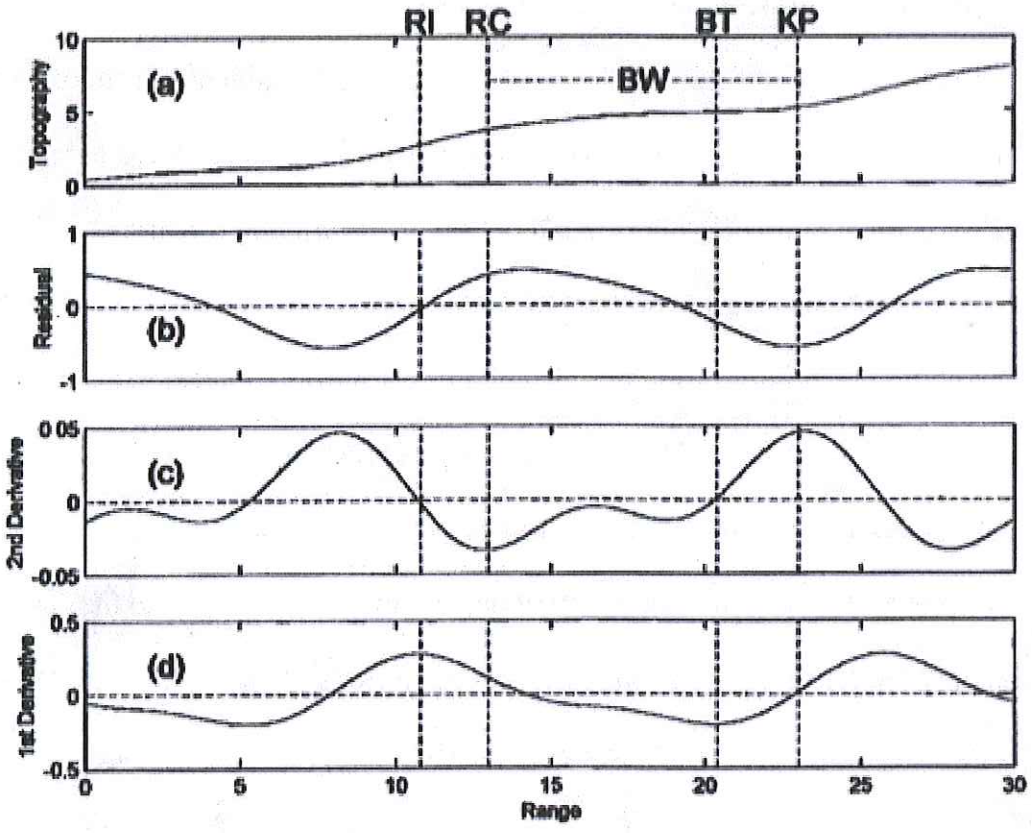

Figure 2.4: Idealized profiles of erosional shoreline elevation and its derivatives, from Hare et al. (2001). (a) Unmodified elevation profile. (b) Elevation with the trend removed. (c) The 2nd derivative, or curvature, of elevation after trend removal. (d) The 1st derivative after trend removal. Abbreviations indicate the riser inflection (RI), riser crest (RC), bench top (BT), bench width (BW) and knick-point (KP); each has a unique relationship to minima and maxima in slope and curvature.

The approach outlined by Hare et al. (2001) improves upon field inspection of the topography because it moderates the subjectivity inherent in visual identification of the knick-point. Nevertheless, ambiguity remains in the variable expression of desired features in slope and curvature.

The greater information content of a stacked elevation profile, which the above-mentioned GPS-RTK method and the DEM extracts provide, lends itself to more robust analyses than those used by Hare et al. (2001). The method can be even further improved by utilizing more of the information content of the profile. The slope and curvature profiles can be treated as a sequence of random variables, and thus the profile information can be more robustly represented using the cross-correlation of pairs of profiles as a function of elevation at the first profile and a "lag", or shift, in elevation of the two profiles. This approach is analogous to cross-correlation techniques used by seismologists to automate picking of seismic phases by calculating time "lags" between arrivals at different locations (Ito, 1985; VanDecar and Crosson, 1990; Shearer, 1997).

A Matlab (Mathworks®, 2010) algorithm was developed to first estimate azimuth of the shoreline from regression for a slope of y vs. x, here denoted as p, in the x-y positions extracted parallel to the shoreline expression. I then transform the x-y map-projected positions for the shoreline-orthogonal (from either GPS-RTK survey or DEM extraction) swath to a Cartesian coordinate system with y'-axis parallel to the shoreline using (Zwillinger, 1996):

$$a = \tan^{-1} p + \frac{\pi}{2} \qquad \text{(Equation 2.1)}$$

$$(x_2, y_2) = \begin{bmatrix} x \\ y \end{bmatrix} \begin{bmatrix} \cos a & \sin a \\ -\sin a & \cos a \end{bmatrix} \qquad \text{(Equation 2.2)}$$

Following transformation I ignore the *y'* coordinate, retaining only *x'*- and *z*-values within averaging intervals, or "bins," at 1-m horizontal sampling orthogonal to the shoreline trace. When the transformation algorithm is used on depositional shorelines, the elevation at the crest of the features is easily observed, along with a standard deviation describing the uncertainty. Thus for depositional shorelines no additional analysis is needed. Erosional shorelines are additionally analyzed with a Matlab (Mathworks®) cross-correlation algorithm to compare two shorelines and estimate the difference in elevation, or "lag", between the two, as described in sections to follow.

Synthetic Testing

In initial stages of development, I constructed a skeletalized pair of synthetic shoreline profiles with a priori-known 5 m elevation lag (Figure 2.5). The first step in the algorithm is to convert the shorelines to their 1st-derivative (slope) profiles. Slope $m = \left(\frac{\partial z}{\partial x}\right)$ appears in the simple equation for a line as:

$$z = mx' + b \qquad \text{(Equation 2.3)}$$

in which *b* is the line intercept. The calculation uses all points within a specified range above and below a target elevation to solve for the desired slope. Because the

expression is linear and we have sufficient sampling density, we can write the observations as an overdetermined system of linear equations, which in matrix form is expressed as (e.g., Menke, 1989):

$$\bar{d} = \bar{\bar{G}}\bar{m} \qquad \text{(Equation 2.4).}$$

Here $\bar{d}$ is a vector containing n elevation measurements z, $\bar{\bar{G}}$ is an nx2 matrix consisting of the n corresponding x' values in the first column and values of 1 in the second column, and $\bar{m}$ is a 2x1 vector containing the unknown parameters of slope m and intercept b.

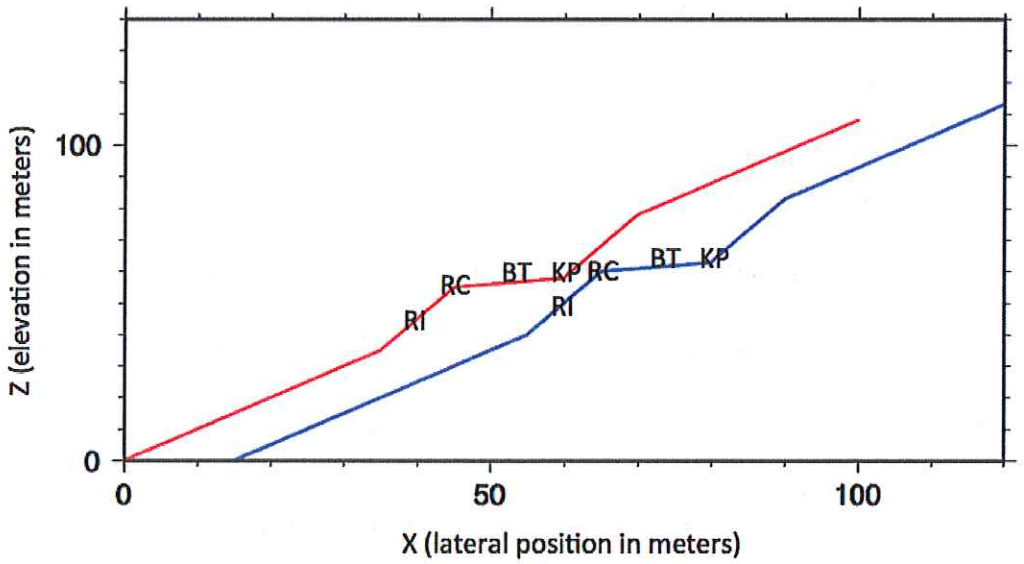

Figure 2.5: Synthetic shoreline profiles. The blue profile was designed with a 5m positive elevation lag.

An overdetermined system of linear equations can be solved via:

$$\bar{m} = \left[\bar{\bar{G}}^T\bar{\bar{G}}\right]^{-1}\bar{\bar{G}}^T\bar{d} \qquad \text{(Equation 2.5)}$$

for the ordinary least squares (OLS) case (Menke, 1989). I invert for slope using this approach at a regular sampling interval of 0.1 m in elevation (z), using all measurements z-measurements within a 1.5 m (horizontally) of each point. The 1st-derivative profiles of the synthetic data of Figure 2.5 are shown in Figure 2.6.

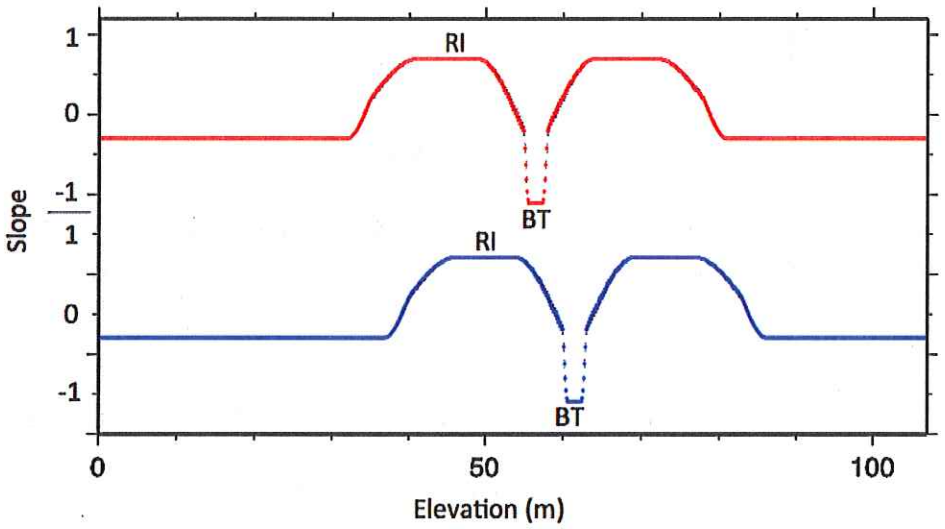

Figure 2.6: 1st derivative (slope) profiles from synthetic data (artificially offset). Minimum slope represents the bench-top (BT) and maximum slope represents the riser inflection (RI) and erosional escarpment. Black bars (barely visible) represent a posteriori error bars for each point.

The calculation of the 2nd-derivative (curvature) is very similar to that for slope. I substitute slope results from Eqn. 2.5 into the $\overline{d}$ vector of Eqn. 2.4 and the regularly sampled heights into the first column of the sensitivity matrix, $\overline{\overline{G}}$, to calculate curvature. The 2nd-derivative profiles of the synthetic data are shown in Figure 2.7.

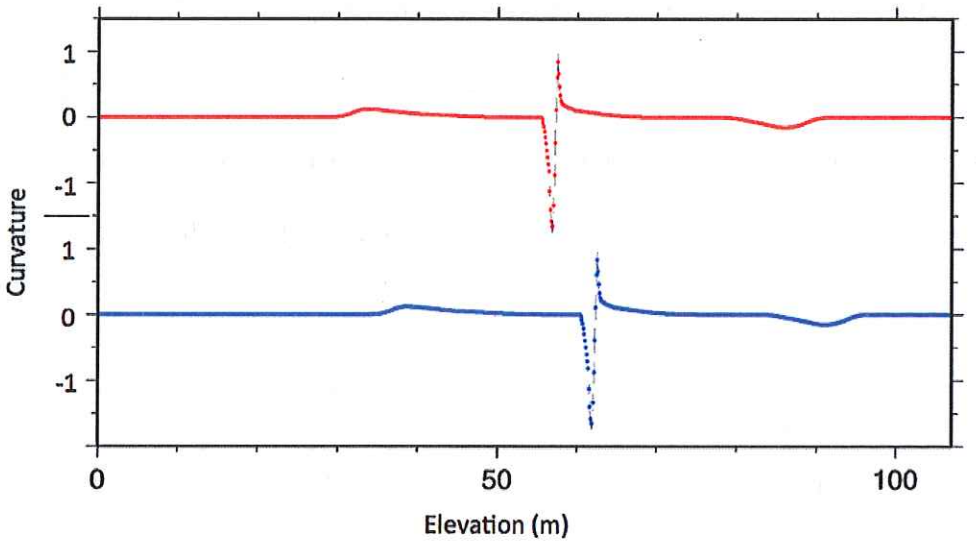

Figure 2.7: 2nd derivative (curvature) profiles from synthetic data. Minimum curvature represents the riser crest (RC) and maximum curvature represents the knick-point (KP). Black bars represent error bars for each point.

For clarification purposes, the riser crest and knickpoint as they are identified in Figure 2.7 are not strictly the true elevation of these features. Since the slope calculation is not a representative of the derivative at a point, but rather an average of the derivative over the specified range, the zone of minimum slope corresponding to the benchtop is narrowed to a ~2-3 m stretch of elevation with ~5+ m of transitional slope to the maxima over the riser and erosional scarp. As a result, the 2nd-derivative (in effect, the "slope of the slope") also has peaks displaced from the elevations where the 2nd-derivative maximum and minimum truly occur. This is irrelevant for the cross-correlation analysis since the same biasing effect is introduced into both profiles. Thus, the elevation and height differences that yield the maximum correlation will reproduce faithfully the elevation and height differences between shorelines, maintaining confidence in the "lag" of maximum correlation, but decreasing confidence in the elevation observed in graphical

representations at which these maximum and minimum correlations occur. For both the slope and curvature profiles, I calculate an a posteriori standard deviation (σ) for each point in order to perform more robust statistical analysis using the following equations (Menke, 1989):

$$\bar{e} = \bar{d} - \bar{\bar{G}}\bar{m} \qquad \text{(Equation 2.6)}$$

$$\sigma = \sqrt{\frac{\left(\bar{e}^T\bar{e}\right)\left(\bar{\bar{G}}^T\bar{\bar{G}}\right)^{-1}}{N-M}} \qquad \text{(Equation 2.7)}$$

where $\bar{e}$ is the error.

I cross-correlate the two profiles for both the slope and curvature. The cross-correlation is calculated by designating one of the profiles as a reference profile, iteratively shifting the other by a specified lag, and then calculating the correlation coefficient using:

$$r_m = \frac{n\sum Y_1Y_2 - \sum Y_1 \sum Y_2}{\sqrt{\left[n\sum Y_1^2 - \left(\sum Y_1\right)^2\right]\left[n\sum Y_2^2 - \left(\sum Y_2\right)^2\right]}} \qquad \text{(Equation 2.8)}$$

where r_m is the (lag-dependent) correlation coefficient, Y_1 is the sequence of either slope or curvature from the reference profile, Y_2 is the same sequence from the shifted profile, and n is the number of samples from the sequence (Davis, 1986). This can be conceptualized as the covariance of the two profiles at the specified lag divided by the product of their standard deviations and ranges from −1 to 1, with zero being completely uncorrelated and one being perfectly correlated. The correlation coefficient is calculated for a broad range of possible lags (in the case of

the synthetic data, from -55 m to 55 m). Correlograms for the synthetic elevation profiles in Figure 2.5 are shown in Figure 2.8.

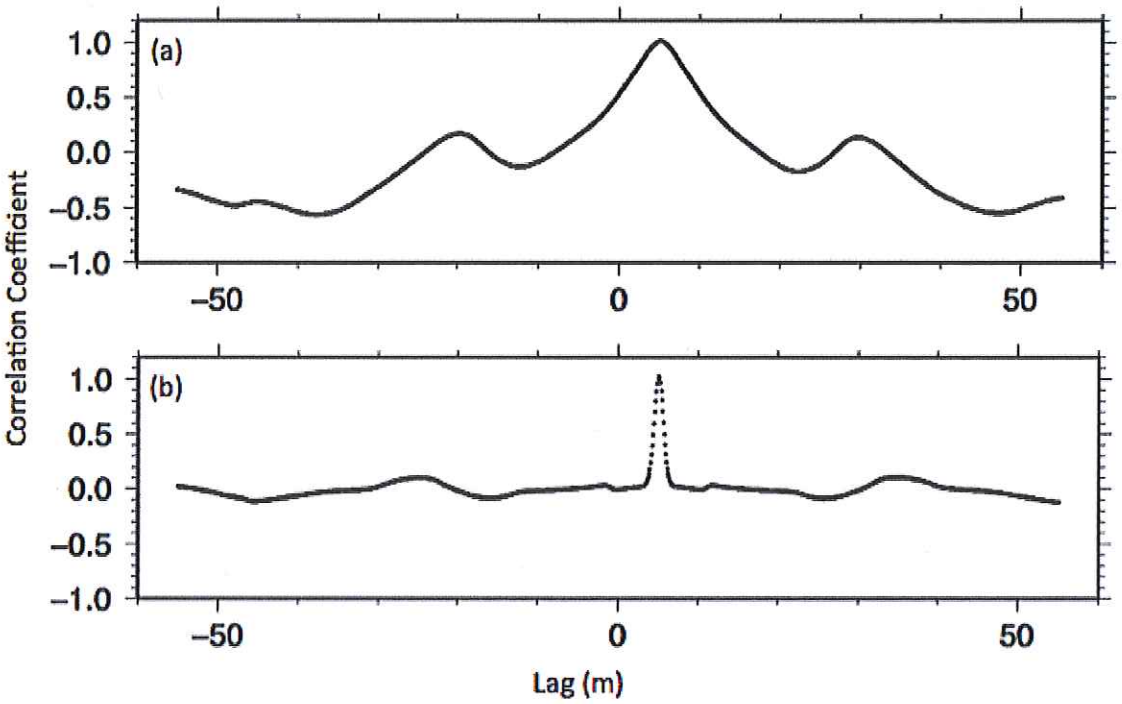

Figure 2.8: Correlogram for (a) slope and (b) curvature calculated from synthetic data. The maximum correlation coefficient (one in each case for the synthetic data) occurs as expected at 5 m.

The two signals used for synthetics are identical except for the difference in height of each of the shoreline features, therefore, the algorithm correctly identifies a perfect correlation of the signals at 5 m lag.

Testing Real Data:

The cross-correlation algorithm next is applied to two shorelines extracted from 2 m resolution DEMs near Lakeside, Utah results in less desired correlations (Figure 2.9).

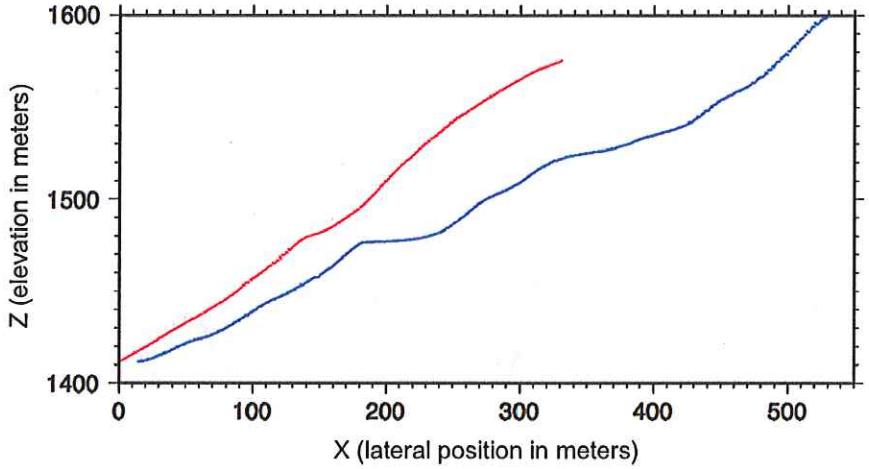

Figure 2.9: Shoreline profiles from 2 m DEMs taken near Lakeside, Utah. The red shoreline is about 4 km north of the blue shoreline, nearer the center of maximum displacement.

Visual inspection of the swath-mean shoreline profiles suggests a shoreline elevation difference of around 2-3 meters with the southern profile slightly lower (Fig. 2.9). This estimate is reinforced by visual inspection of the 1st- and 2nd-derivative profiles (Figures 2.10 and 2.11, respectively). The correlogram (Figure 2.12), however, do not behave similarly to those of the synthetic data.

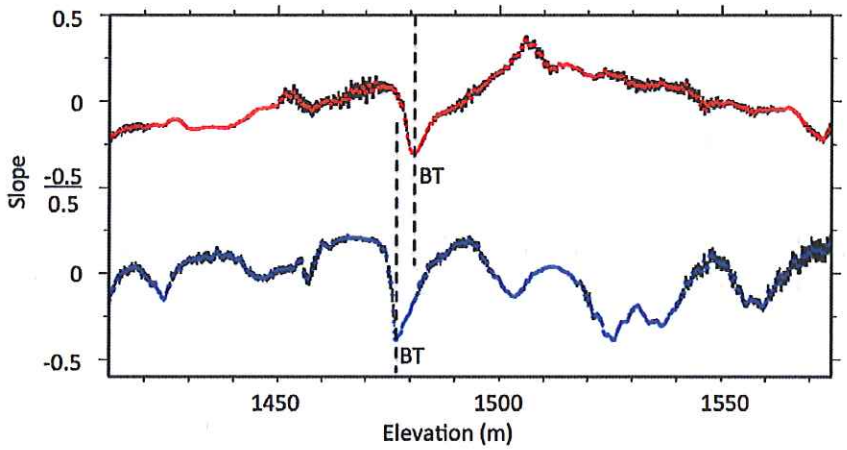

Figure 2.10: Slope profiles of the shorelines depicted in Figure 2.8. Bench-top (BT) minima indicated in the profiles suggest a difference of ~5 meters.

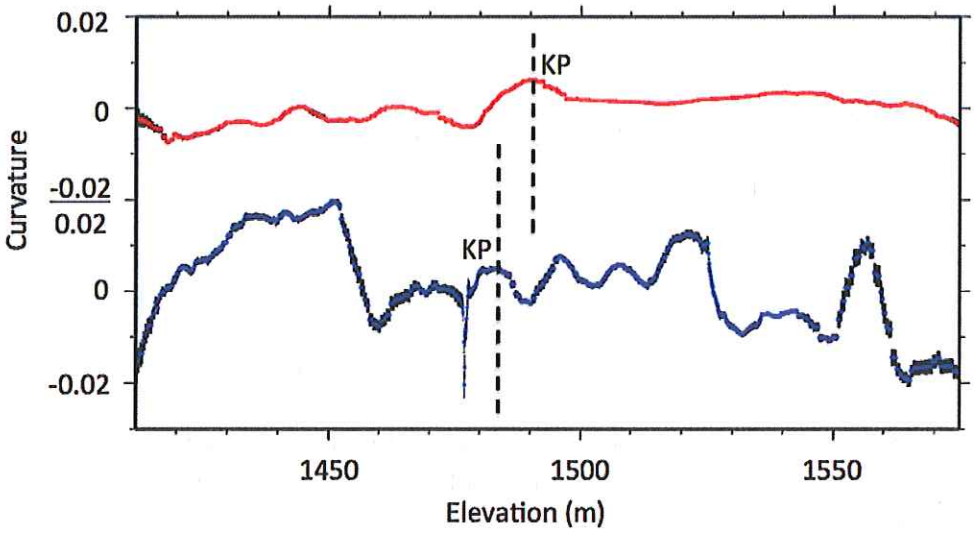

Figure 2.11: Curvature profiles of the shorelines depicted in Figure 2.8. Knick-points (KP) indicated by the profiles vary by ~5 meters.

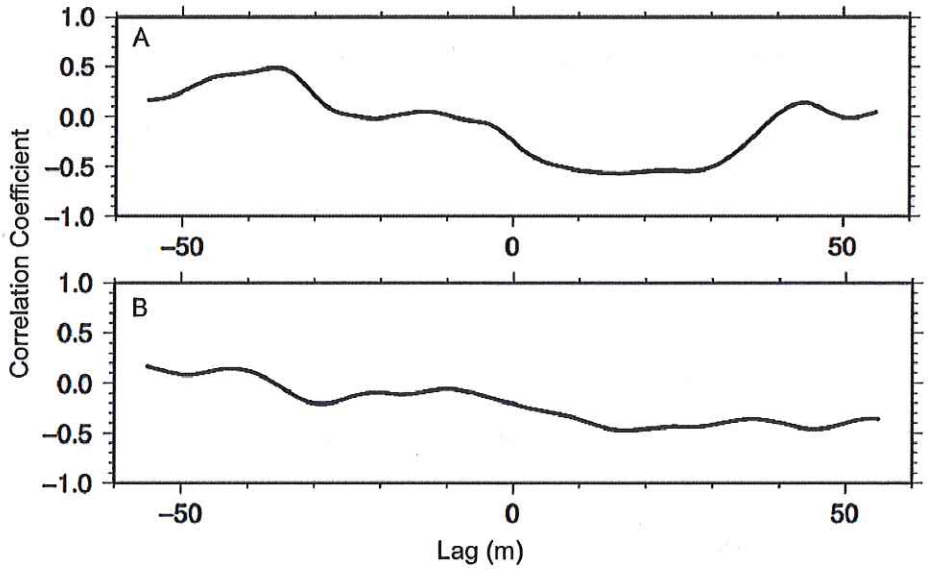

Figure 2.12: Correlogram for (a) slope and (a) curvature from shorelines near Lakeside, Utah. These correlograms do not have maxima at the anticipated 2- to 5-m lag.

The correlations are weak at the ~5 m lag where the shoreline height change is visually apparent. This is due to differences in length scales of features such as

bench width and additional signals (which act as "noise" for our purposes) present in real paleoshoreline elevation data. Because the cross-correlation estimates average over the entire length of both profiles at each lag, the correlation coefficient covers much more than the ~20-30 m height range of an individual shoreline, and hence the desired signal can be overwhelmed by other noise fields. Consequently, it is necessary to isolate the shoreline signals by reducing the "window" of height within which the cross-correlation is calculated. To isolate the shoreline signal, I modified the algorithm to compare profiles within 40 m elevation windows that are moved up and down the range of profile elevation at 10 cm increments. Thus the cross-correlation varies both with lag and elevation corresponding to the center of the window on the reference profile. Figures 2.13a and 2.13b are contour plots for slope and curvature, respectively, in which the 40 m elevation windows are shifted by ±55 m lag.

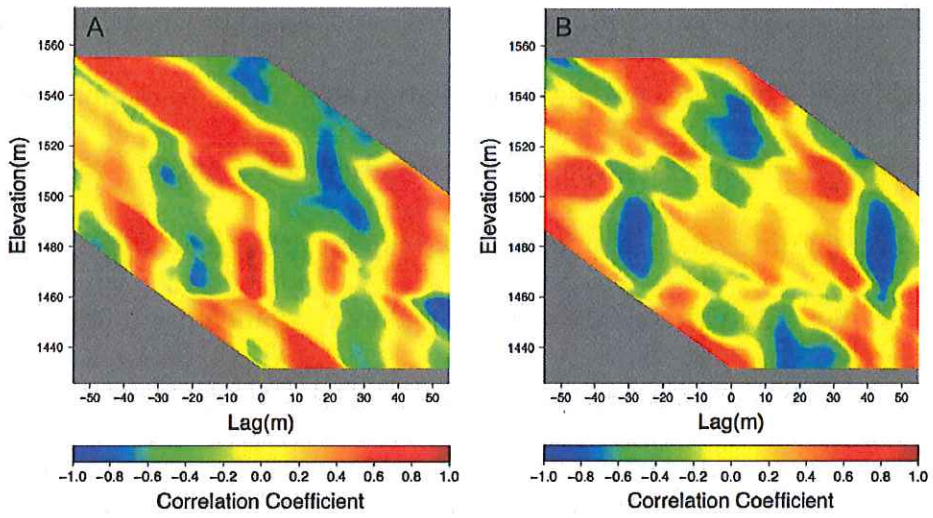

Figure 2.13: Contour plots of windowed cross-correlation of (A) slope and (B) curvature profiles in Figures 2.9-2.11. Correlation coefficients are enhanced, and the slope correlations are strong at about −4 m lag in the 1460-1485 m elevation range. The curvature plot exhibits lower correlation coefficients, but favors elevations at the upper end of the range indicated by the slope correlation contours.

To further improve the constraint of shoreline elevation difference, I stack the slope and curvature correlograms (i.e., average them; Figure 2.14). This helps to downweight correlations of random signals that are not associated with the shoreline process while enhancing high correlation coefficients for slope and curvature where they are in agreement. The intervals for 65% (α_{65}) and 95% (α_{95}) confidence are calculated from the inverse *F*-distribution via the equations:

$$\mathcal{F}_{1-\alpha}^{-1} = 1 + \frac{m * \mathcal{F}^{-1}\left((1-\alpha), m, n\right)}{n-m} \qquad \text{(Equation 2.9)}$$

$$\alpha_n = 1 - \left(\mathcal{F}_{1-\alpha}^{-1}\left(1 - C_{\max}\right)\right) \qquad \text{(Equation 2.10)}$$

where *m* is the number of parameters (two, corresponding to the shoreline elevation of the first profile and the shoreline elevation difference of the two profiles), *n* is the number of observations (i.e., elevation measurements included in calculation of the correlation coefficient), and C_{max} is the maximum correlation coefficient. I plot the contour of correlation coefficient corresponding to each confidence interval for a visual representation of the possible range of estimates, and retain the estimates of uncertainty as part of the estimation procedure.

Fig. 2.14a also exhibits high correlation coefficients at other lags and elevations besides the parameters that I selected as representative of shoreline height variation, and in some cases these may actually be higher than the selected maximum. This is attributed to surface processes that are ubiquitous throughout the basin that in some instances will produce a slope and/or curvature signal on the residual slopes that are similar between locations. We distinguish these from

shoreline signals by examining the raw elevation, slope and curvature profiles prior to cross-correlation analysis and a range of elevation and lag in which the shoreline signal can reasonably be expected to occur. When estimating confidence intervals, we include only the vicinity of the maxima falling with that range.

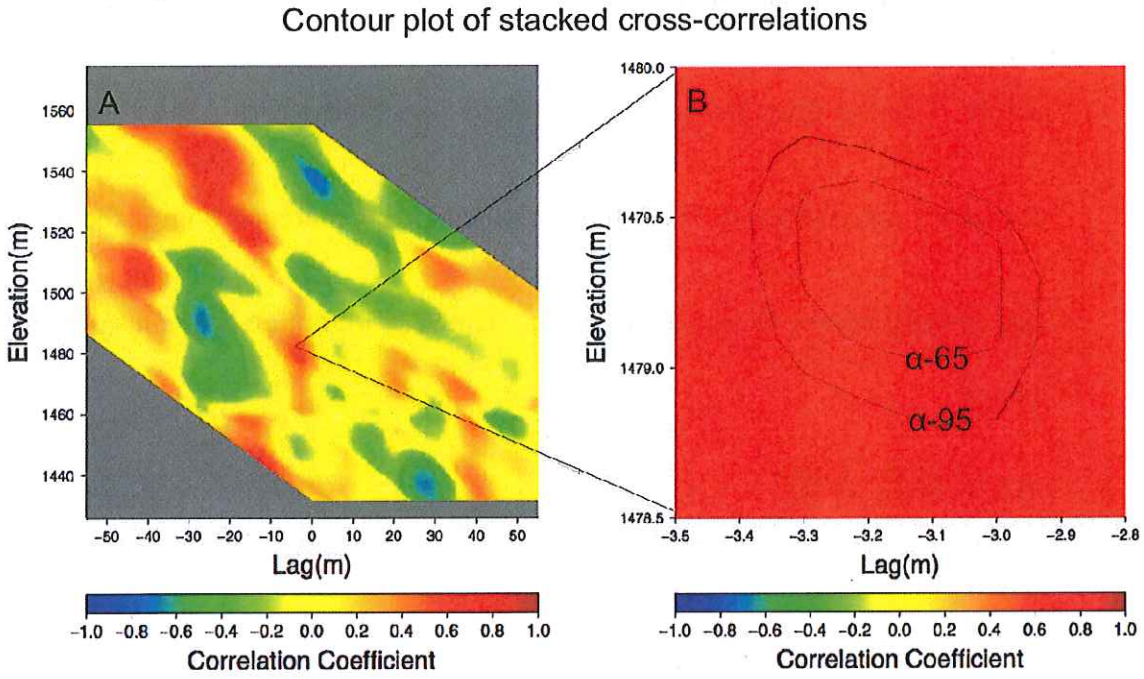

Figure 2.14: (A) Contour plot of stacked 1st and 2nd derivative windowed cross-correlations. (B) 65% and 95% confidence intervals of the estimates. Maximum Correlation coefficient for this shoreline was C_{max}=0.6222; correlation coefficients corresponding to α_{65}=0.6218; α_{95}=0.6209.

Modifications to Optimize the Method

Weighted Least Squares Inversion

I explored several modifications of the method described above to examine whether the changes would increase robustness of the algorithm and minimize cross-correlations of topographic processes unrelated to shoreline formation. I first modified the technique to invert for slope and curvature using a weighted least

squares (WLS) method instead of the ordinary least squares described above. In the slope case, a weighting matrix $\left(\bar{\bar{W}}\right)$ is constructed as a diagonal *n*x*n* matrix where *n* is the size of the *x'*- and *z*-vectors used to invert for each slope estimate. The weight matrix is zero off-diagonal and has diagonal terms consisting of $\frac{1}{\sigma_{i\,z}^2}$, where σ_i is the standard deviation of elevations falling within the i^{th} bin. For curvature estimation, the diagonal of the weighting matrix is composed of $\frac{1}{\sigma_{i\,slope}^2}$ as calculated from the inversion for slope. The WLS inversion is given by (Menke, 1989):

$$\bar{m} = \left(\bar{\bar{G}}^T \bar{\bar{W}} \bar{\bar{G}}\right)^{-1} \bar{\bar{G}}^T \bar{\bar{W}} \bar{d} \qquad \text{(Equation 2.11).}$$

When 2m resolution DEM data are used, weighted least squares inversion for slope and curvature produces smooth curves with recognizable expressions of shoreline features.

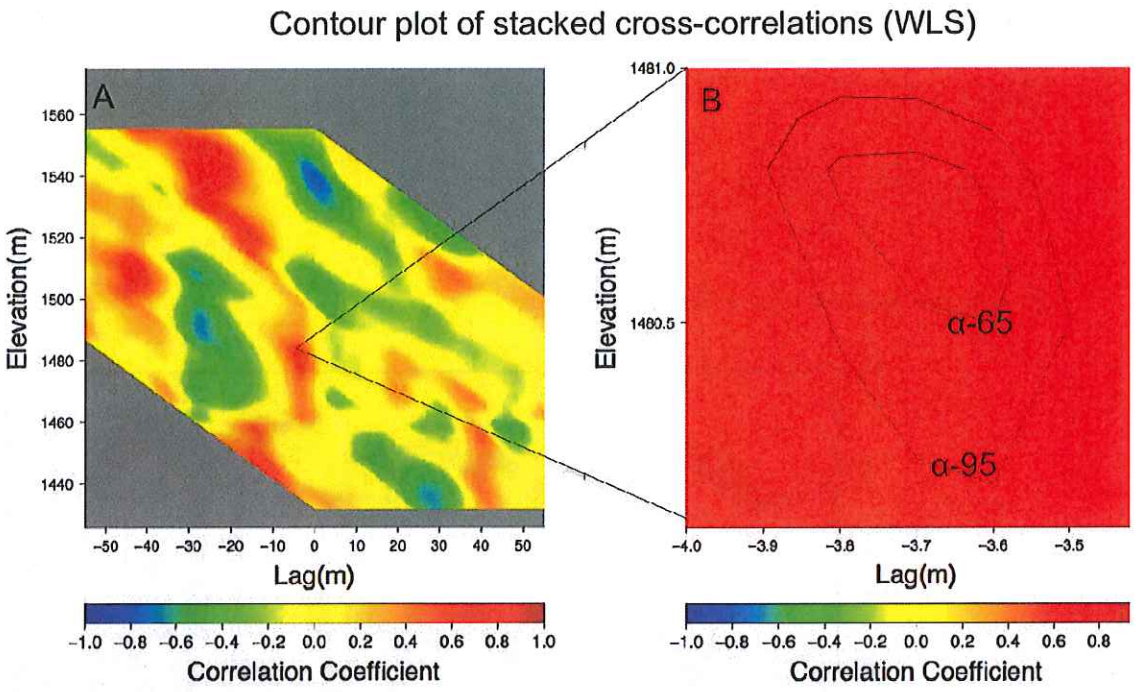

Figure 2.15: (A) Contour plot of stacked 1st-and 2nd-derivative cross-correlations using the WLS method of inversion for slope and curvature. (B) 65% and 95% confidence intervals of the estimates. Maximum correlation coefficient C_{max}=0.6655; correlation coefficients corresponding to confidence intervals α_{65} =0.6651; α_{95} =0.6643 are slightly higher than for the ordinary least squares solution.

Bootstrap Re-Weighting

Derivative operations tend to amplify whatever noise is present, so when applied to 5-m resolution data, the estimates can be discontinuous and highly erratic. Examples of such behavior are shown in Figures 2.16 and 2.17. To reduce noise in derivatives of sparsely-sampled DEMs, I developed a bootstrap reweighting method to augment the WLS inversion for slope. The method integrates the estimated slope via equation 2.10 at 0.1 m increments of elevation:

$$\Delta x'_i = \frac{z_i - z_{i-1}}{m_{i-1}} \qquad \text{(Equation 2.12)}$$

and then interpolates new estimates of x' via equation 2.11 for every original z value:

$$x'_i = x'_{i-1} + \frac{(z_i - z_{i-1})(x'_{i+1} - x'_{i-1})}{(z_{i+1} - z_{i-1})} \qquad \text{(Equation 2.13)}$$

yielding a revised elevation profile.

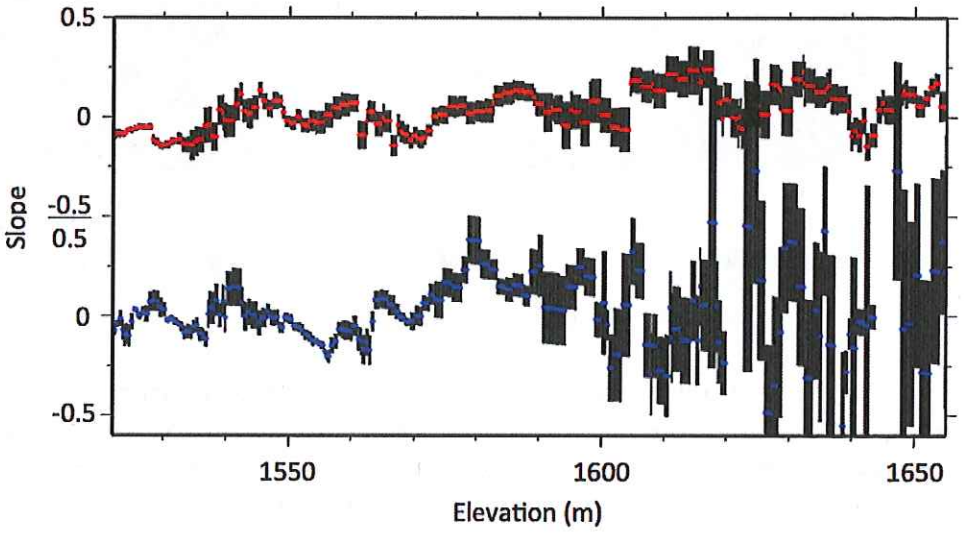

Figure 2.16: Slope profiles of two Cache Valley shorelines from 5-m resolution DEMs. The red profile is near Richmond, Utah and the blue profile is near Providence Canyon.

The misfit between measured x' and the integrated profile is squared and compared to the variance of binned measurements at each z. Where the squared misfit is smaller than the variance, the variance is left unchanged; elsewhere the variance is re-assigned a value equal to the squared misfit.

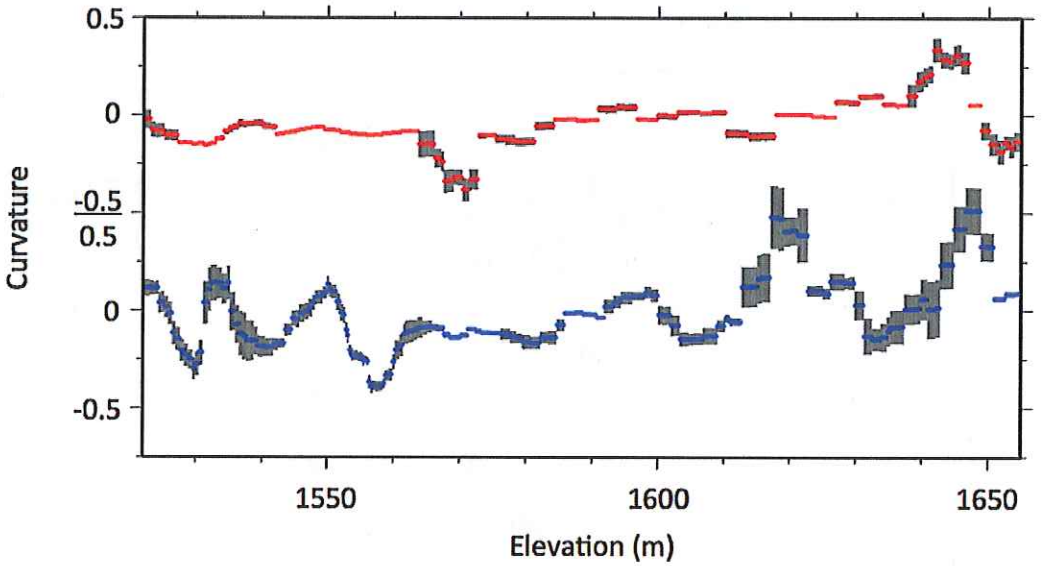

Figure 2.17: Curvature profiles of two Cache Valley shorelines from 5-m resolution DEMs. The red profile is near Richmond, Utah; the blue profile is near Providence Canyon.

The weighted least squares inversion for slope is recalculated, thus down-weighting profile elevations with large misfits to the integrated elevation profile. The change in weighting affects the WLS inversion of curvature as well, via the weighting of parameter variance in equations 2.6 and 2.7.

I tested two different approaches to reweighting. In the first approach (Bootstrap 1), the observed values of x' and z are used with the modified weight matrix to invert for slope. In the second approach (Bootstrap 2), the integrated approximation of x' is used along with the observed values of z with the modified weight matrix to invert for slope.

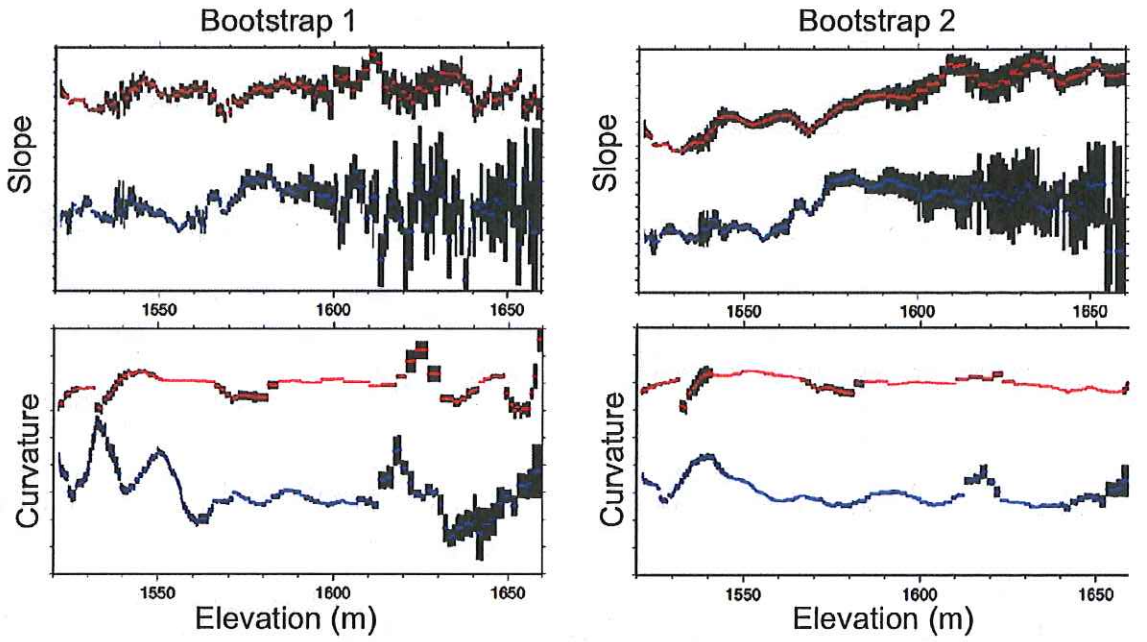

Figure 2.18: Comparison of the slope and curvature profiles for the Bootstrap 1 and Bootstrap 2 re-weighting methods.

Fig. 2.18 demonstrates the smoothing effects and reduction in noise for each of the bootstrap re-weighting methods. Bootstrap 2 appears to have a more significant smoothing effect. The risk involved with this re-weighting method is that some important signals may be attenuated by using the integrated shoreline profile instead of actual topographic measurements.

Wiener Filtering

I also tested a Wiener filter to assess whether this might improve robustness. Wiener filtering seeks to design an optimal filter for which the output signal is statistically similar to some "desired" signal (in this case, a signal with minimal noise). I approximate the noise statistics as the difference between the x' estimates

in the original elevation profile and x' integrated from the derived slope profile, as previously described (equations 2.12 and 2.13). The filter, H, is derived in the spectral domain using the autopower spectrum of the misfit, S_{vv}, and the autopower spectrum of the x' signal , S_{xx}, via:

$$H(\Omega) = \frac{S_{xx}(\Omega) - S_{vv}(\Omega)}{S_{xx}(\Omega)} \qquad \text{(Equation 2.14)}$$

The filtered signal is determined by multiplying the Fourier transform of the observed signal by the transfer function (wiener filter) in the spectral domain, and inverse-transforming to the spatial domain. The slope profile is then derived by inverting for slope using the filtered x' values with the observed z values by the WLS method.

Methodological Comparison

In total, I developed four different algorithms to estimate first- and second-derivatives of shoreline elevations (here referred to as WLS, Bootstrap 1, Bootstrap 2, and the Wiener filter). I tested the methods by applying them to 5-m DEM data and comparing to results derived from 2-m DEM data at the same location, to determine which of the approaches produced the most robust results. Erosional shoreline data were extracted from both 2-m resolution DEMs and 5-m resolution DEMs using identical polygon features for a mask in ArcMap. I compared shoreline height and height difference estimates from each method at three 2-m resolution shorelines. I triangulate these sites by summing the lag estimates for all three independent shoreline pair perturbations for the three sites. If the triangle closes (i.e., the lags sum to zero within uncertainties) for a given algorithm, the

approach can be considered viable for the less challenging problem of estimating shoreline heights from 2-m resolution data. For this comparison, I use eight shoreline profiles with locations represented in Fig. 2.19. Examining the 2-m data first also establishes a baseline for what the "true" shoreline height variation should be prior to examining how the methods perform when applied to the 5-m resolution profiles. The shoreline data are cross-correlated with data from another shoreline location using each of the four cross-correlation methods. When applied to profiles extracted from 2-m resolution data, I found that in many cases one of the four methods produced outliers and estimates inconsistent with the other three, and the outlier was not always produced by the same method. None of the four methods triangulated within uncertainties in every instance. To quantify the performance of each method, I calculate the weighted mean of estimates from the other three methods with χ^2 normalized standard deviation and plot the fourth method as an outlier to visually observe which method, if any, when excluded improves the error estimates most substantially. The weighted-mean of three measurements is given by:

$$lag_{mean} = \frac{\frac{1}{\sigma_1^2} lag_1 + \frac{1}{\sigma_2^2} lag_2 + \frac{1}{\sigma_3^2} lag_3 + \frac{1}{\sigma_4^2} lag_4}{\frac{1}{\sigma_1^2} + \frac{1}{\sigma_2^2} + \frac{1}{\sigma_3^2} + \frac{1}{\sigma_4^2}} \qquad \text{(Equation 2.15)}$$

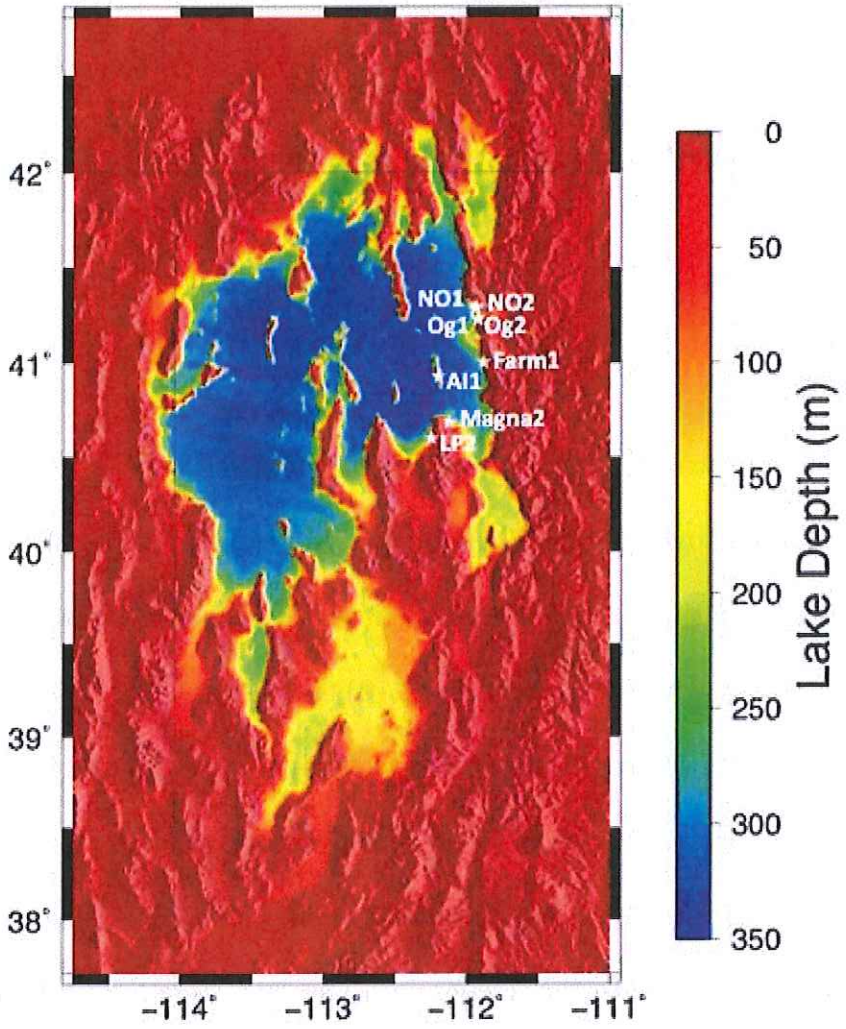

Figure 2.19: Profile locations used for testing the four cross-correlation approaches.

Parameter error estimates derived from confidence intervals via equation 2.7 can overestimate or (more often) underestimate the true uncertainties if noise processes are correlated or non-Gaussian. Both of these are likely to be true of shoreline elevation features. An independent estimate of the errors associated with these approaches can be calculated from the closure of lag estimates from combinations of three shorelines:

$$misfit_{1\,RMS} = \sqrt{\frac{\left|lag_1 - lag_2\right|^2 + \left|lag_1 - lag_3\right|^2}{2}} \qquad \text{(Equation 2.16)}$$

The resulting RMS misfits are used to calculate the χ^2 parameter,

$$\chi^2 = \frac{\sum_{i=1}^{N} \frac{e_i^2}{\sigma_i^2}}{(N-M)} \qquad \text{(Equation 2.17)}$$

$$e = misfit_{RMS}$$

which should scale to one. The comparison of misfits to predicted parameter error when summed over all possible triangles (i.e., a large number of measurements N) thus yields a scaling factor for the estimates of measurement uncertainty derived from confidence intervals (equation 2.10) that better reflects uncertainties associated with colored-noise processes likely to be encountered in geomorphological features. From this, I determined that for 2m data, none of the methods improves the error estimates when excluded over the other three methods substantially enough to decisively reject it as a valid method. I then compare the results for using 2-m resolution data to those using 5-m resolution data (Fig. 2.21). From Figure 2.21, it is apparent that when comparing only lags, the error estimates from 2-m and 5-m resolution data only overlap about half the time from the points used.

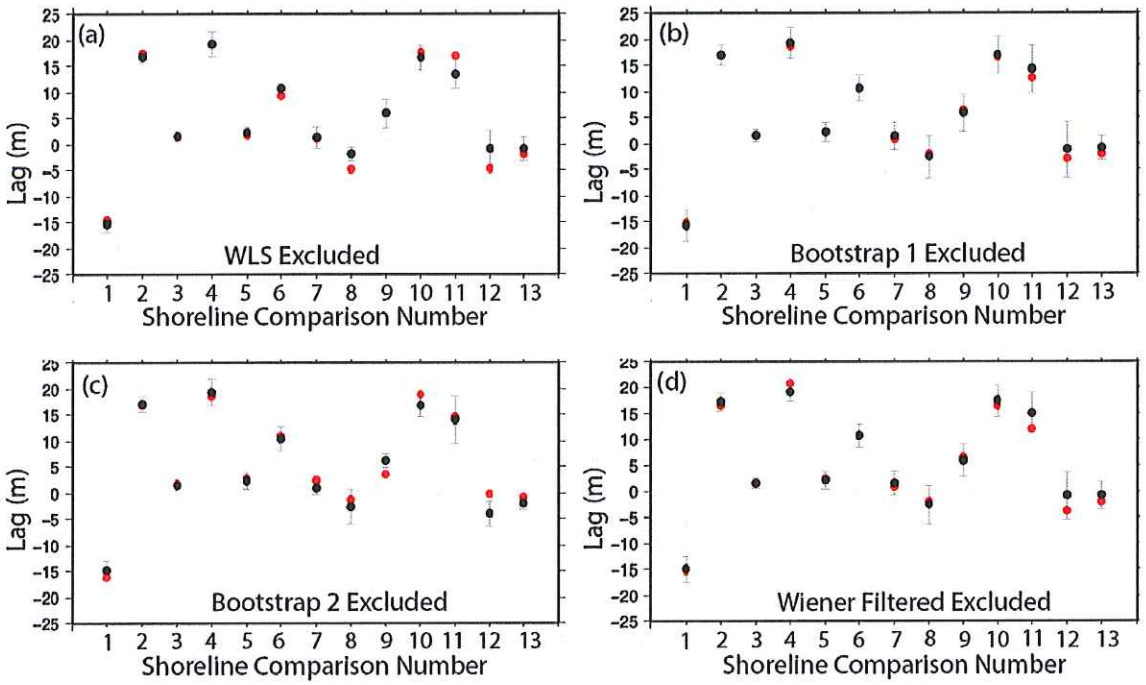

1 - Al1_2 & Magna2_2
2 - Farm1_2 & Al1_2
3 - Farm1_2 & Magna2_2
4 - NO1_2 & Al1_2
5 - NO1_2 & Farm1_2
6 - NO1_2 & LP2_2
7 - NO1_2 & Magna2_2
8 - NO1_2 & NO2_2
9 - NO1_2 & Og1_2
10 - NO1_2 &)g2_2
11 - Og1_2 & Al1_2
12 - Og1_2 & Farm1_2
13 - Og1_2 & Magna2_2

Figure 2.20: Weighted means (black) with χ^2 normalized standard deviation of three methods with the fourth excluded (red). (A) WLS method excluded; (B) Bootstrap 1 method excluded; (C) Bootstrap 2 method excluded; (D) Wiener filtered method excluded.

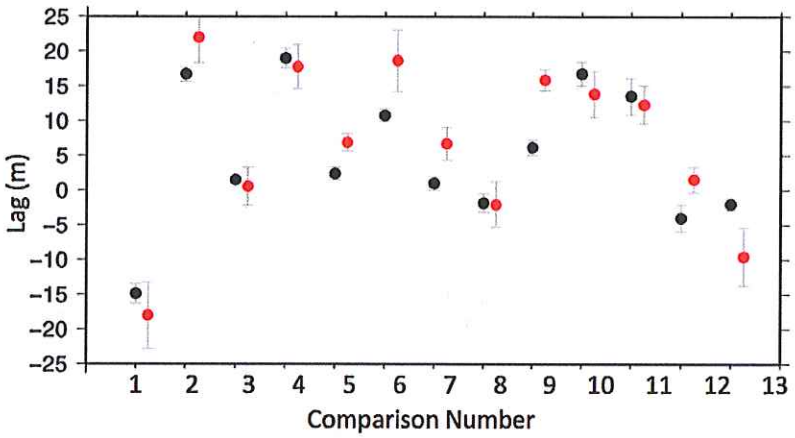

Figure 2.21: Comparison of weighted means of lag using 5-m resolution data (red) and 2-m resolution data (black).

The next step is to estimate shoreline elevations from the lag data. This is done here by setting the shoreline AI1, which corresponds to a location on the south side of Antelope Island and is in close proximity to Currey's (1982) point # 29 in the his Bonneville dataset, as a baseline with known elevation of 1602 m. Lags are calculated for all shorelines that are directly compared to this shoreline directly from the estimate of lag. The uncertainty is the 95% confidence interval. For shorelines that are not directly compared to the baseline, the shoreline is cross-correlated with another that is cross-correlated with the baseline. In this case, the uncertainty is the sum of the 95% confidence intervals for each of the shorelines. The shoreline elevations correlate more closely between the 2-m and 5-m resolution data overlapping errors with Farm1 being the only exception which is within 40 cm of overlapping (Fig. 2.22).

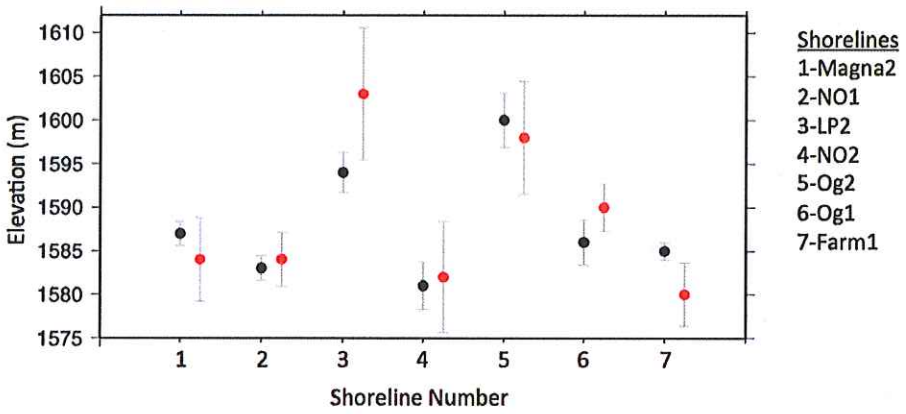

Figure 2.22: Comparison of shoreline elevation estimates and sigma 2 confidence intervals taken from lags using 5-m resolution data (red) and 2-m resolution data (black).

Discussion

With only one exception, the 2σ uncertainties of elevation estimates from 5-m data overlap those from 2-m data. The shoreline estimates also triangulate within error in all cases for which triangulation has been performed. The uncertainties from 2-m resolution data, the largest of which are around 3 m, indicates 2-m resolution data results in adequate measurements for application in isostatic analysis. Repeatability of the 2-m data is sufficiently robust to suggest that estimates derived from those data are reliable. The 5-m data, on the other hand, generally produces much larger uncertainties, with the largest exceeding 7 m. With the sparseness of data, this is expected. Thus the method may not be precise enough for use in isostatic rebound studies when applied to 5-m sampled data. However, by weighting the shoreline elevation data by the inverse variance of each sample, t 5-m data may still be useful. The data acquired via GPS-RTK was sampled densely

enough in the surveys that I collected to produce results similar to the results obtained using 2-m resolution data. I foresee that for uses that require higher resolution in a relatively small area, this will be the preferred method of data collection as the sampling rate can be more tightly controlled.

The hope is that others in the scientific community will find this method of comparing breaks in topography useful as well. It may be useful for other applications such as quantifying differences in surface offset of fault scarps. This method may enable researchers to estimate the differences in scarp offset with greatly reduced cost, labor and environmental impact relative to trenching.

By estimating shoreline elevation lags from the weighted average of at least three cross-correlation methods as described above (WLS, Bootstrap 1, Bootstrap 2, and Wiener filtered), I conclude that with 2-m resolution data, the resulting lags and their associated standard deviations can be accepted with confidence. With 5-m resolution data, the results can be accepted, but the standard deviation is often so large as to minimize usefulness. If weighted by the inverse variance, these estimates will not negatively affect inversions for isostatic parameters. By using sufficient caution in the acquisition of shoreline data as well as analysis of the data, this methodology is effective, and is applicable to other studies requiring estimates of variations in elevations of topographic breaks.

References

AGRC, Utah Automated Geographic Reference Center, http://gis.utah.gov/, accessed 2010-2012.

Bard, E., B. Hamelin, R.G. Fairbanks, and A. Zindler, Calibration of the ^{14}C timescale of the past 30,000 years using mass spectrometric U-Th ages from Barbados corals, *Nature, 345*, 405-410, 1990.

Barrientos, S.E., R.S. Stein, and S.N. Ward, Comparison of the 1959 Hebgen Lake, Montana and the 1983 Borah Peak, Idaho, earthquakes from geodetic observations, *Bull. Seismol. Soc. Am., 77*, 784-808, 1987.

Benson, L.V., S.P. Lund, J.P. Smoot, D.E. Rhode, R.J. Spencer, K.L. Verosub, L.A. Louderback, C.A. Johnson, R.O. Rye, and R.M. Negrini, The rise and fall of Lake Bonneville between 45 and 10.5 ka, *Quat. Intern., 235*, 57-69, 2011.

Bills, B.G., D.R. Currey, and G.A. Marshall, Viscosity estimates for the crust and upper mantle from patterns of lacustrine shoreline deformation in the Eastern Great Basin, *J. Geophys. Res., 99*, pp. 22,059-22,086, 1994.

Crittenden, M.D., Jr., Effective viscosity of the Earth derived from isostatic loading of Pleistocene Lake Bonneville, *J. Geophys. Res., 68*, 5517-5530, 1963.

Crittenden, M.D., Jr., Viscosity and finite strength of the mantle as determined from water and ice loads, *Geophys. J. R. Astron. Soc., 14*, 261-279, 1967.

Currey, D.R., Lake Bonneville: Selected features of relevance to neotectonic analysis, *U.S. Geol. Surv. Open-File Rep., 82-1070*, 31 pp., 1982.

Currey, D.R., Quaternary paleolakes in the evolution of semidesert basins, with special emphasis on Lake Bonneville and the Great Basin, *Paleogeogr. Paleoclimatol. Paleoecol., 76*, 189-214, 1990.

Davis, J.S., *Statistics and Data Analysis in Geology*, 646 pp., John Wiley & Sons, New York, 1986.

ESRI®, ArcGIS, version 10, http://www.esri.com/, 2010-2012.

Gilbert, G.K., Lake Bonneville, *U.S. Geol. Surv. Monogr., 1*, 438 pp., 1890.

Godsey, H.S., D.R. Currey, and M.A. Chan, New evidence for an extended occupation of the Provo shoreline and implications for regional climate change, Pleistocene Lake Bonneville, Utah, USA, *Quatern. Res., 63,* 212-223, 2005.

Godsey, H.S., C.G.Oviatt, D.M. Miller, and M.A. Chan, Stratigraphy and chronology of offshore to nearshore deposits associated with the Provo shoreline, Pleistocene Lake Bonneville, Utah, *Palaeogeogr. Palaeoclimatol. Palaeoecol., 310*, 442-450, 2011.

Google®, Google Earth, version 6.0, http://kh.google.com/, 2011-2012.

Hare, J.L., J.F. Ferguson, L.V. Aiken, and J.S. Oldow, Quantitative characterization and elevation estimation of Lake Lahontan shoreline terraces from high-resolution digital elevation models, *J. Geophys. Res., 106*, 26,761-26,774, 2001.

Ito, A., High resolution relative hypocenters of similar earthquakes by cross-spectral analysis method, *J. Phys. Earth, 33*, 279-294, 1985.

Janecke, S.U., and R.Q. Oaks Jr., New insights into the outlet conditions of late Pleistocene Lake Bonneville, southeastern Idaho, USA, *Geosphere, 7*, 1369-1391, 2011.

Lemons, D.R., M.R. Milligan, and M.A. Chan, Paleoclimatic implications of late Pleistocene sediment yield rates for Bonneville Basin, northern Utah, *Paleogeogr. Paleoclimatol. Paleoecol., 123*, 147-159, 1996.

MathWorks®, Matlab & Simulink, version R2010a, http://www.mathworks.com/, accessed 2010-2012.

Menke, W., *Geophysical Data Analysis: Discrete Inverse Theory*, 289 pp., Academic Press, San Diego, CA, 1989.

Nishizawa, S., *The Bonneville Lake Basin Shoreline Records of Large Lake and Abrubt Climate Change Events*, 150 pp., University of Utah, Salt Lake City, UT, 2010.

O'Connor, J.E., Hydrology, hydraulics, and geomorphology of the Bonneville Flood, *Geol. Soc. Am., Special Paper 274*, 83 pp., 1993.

Shearer, P.M., Improving local earthquake locations using the L1 norm and waveform cross-correlation: Application to the Whittier Narrows, California, aftershock sequence, *J. Geophys. Res., 102*, 8269-8283, 1997.

VanDecar, J.C., and R.S. Crosson, Determination of teleseismic relative phase arrival times using multi-channel cross-correlation and least squares, *Bull. Seismol. Soc. Am., 80*, 150-169, 1990.

Zwillinger, D., *Standard Mathematical Tables and Formulae, 30th Edition*, 812 pp., CRC Press, Inc., Boca Raton, FL, 1996.

CHAPTER 3

MODELING ISOSTATIC RESPONSE WITH NEW ESTIMATES OF BONNEVILLE SHORELINE ELEVATIONS

Abstract

Pleistocene Lake Bonneville has long been considered an ideal location for modeling flow rheology. However, lower crustal and other depth dependence of flow is poorly resolved by existing data, in part because paleolake shoreline deformation is sparsely sampled in time and space. In the previous chapter I described a new approach to measuring shoreline elevations. In this chapter, I model isostatic response to Bonneville unloading as an elastic layer over a fluid half-space, and compare results with and without denser sampling afforded by new measurements. I first compare observed uplift and the modeled response to unloading of an elastic plate over an inviscid asthenosphere as a function of assumed effective elastic thickness (T_e). The best-fit T_e for the Bonneville uplift is 25±2 km using only shoreline elevation estimates compiled previously and 26±2 km when these are augmented with 44 new measurements. No new measurements are collected for subsequent lake levels, but the best-fit T_e for the Provo uplift is 17±3 km, and Gilbert level measurements are relatively insensitive to T_e. I then model shoreline uplift in response to the entire history of loading and unloading, assuming an elastic plate over an isoviscous viscoelastic asthenosphere. This approach assumes parameters remain unchanged throughout the loading history, and yields a best-fit model with T_e=70±5 km and viscosity η=~2x10^{18} Pa s with 95% confidence

ranging from ~1x10^{18} Pa s to ~5x10^{19} Pa s when only prior measurements are used. With the newer data added, the best-fit model has T_e=58±2 km and η ranging from ~1x10^{18} Pa s to ~1x10^{19} Pa s with 95% confidence. The 12-15 m weighted root-mean-square misfit to the best-fitting models are dominated by tectonic signals related to Basin-and-Range tectonics, particularly seismic offsets of the Wasatch fault, and closely mimics the geological timescale pattern of basin-subsidence and range-uplift.

Introduction

Pluvial Lake Bonneville covered a significant portion of western Utah along with small portions of eastern Nevada and southern Idah during the last glacial maximum (Fig. 3.1). During the Bonneville epoch (the maximum level the lake attained), the lake covered a more than 52,000 km^2 area to depths exceeding 360 meters (Bills et al., 1994). The mass of the load imposed by the water during this time was around 10^{17} kg. Under this load, the lithosphere subsided by up to 76 meters. Most of that subsidence has been recovered following draining and drying of the lake, and ~76 meters of lake rebound is recorded as differences in elevation of preserved shoreline features. Elevations of the remnant shorelines of Pleistocene Lake Bonneville are a direct observation of isostatic response that can be used to model rheological properties of the lower crust and upper mantle. Bonneville is arguably one of the best field laboratories globally for this purpose owing to excellent preservation of multiple shorelines (Schofield et al., 2004) and

increasingly accurate radiometric dating of those shorelines (Bard et al., 1990; Godsey et al., 2011; Benson et al., 2011; Janecke and Oakes, 2011).

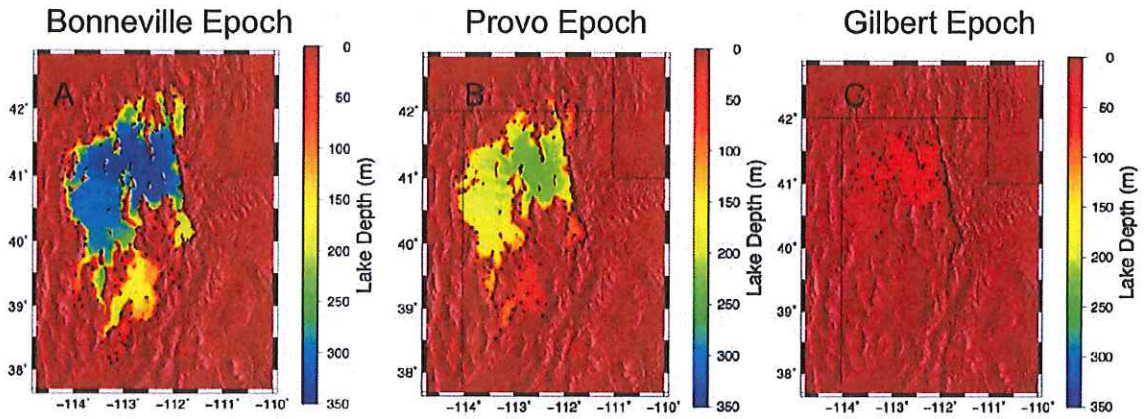

Figure 3.1: Lake depths during the three main levels of Lake Bonneville, estimated by subtracting modern topography from paleoshoreline elevation data points (Currey, 1982). (A) Bonneville epoch (~17.8-17.4 ka); (B) Provo epoch (~17.4-15.2 ka); (C) the Gilbert epoch (~12.5-11.5 ka).

Pluvial lake rebound provides less ambiguous constraint of stress forcing than glacial rebound because of the difficulty of determining the paleoheight (and often the lateral extent) of continental glaciers. Pluvial lake shorelines, by contrast, unambiguously define the water depth and hence the load. As lake surface elevations of Lake Bonneville stabilized at various levels, individual shorelines were formed on horizontal (equipotential) surfaces (Gilbert, 1890; Crittenden, 1963, 1967; Walcott, 1970; Passey, 1981; Nakiboglu and Lambeck, 1983; Bills and May, 1987; Bills et al., 1994; Janecke & Oakes, 2011). Rebound of the shorelines following

removal of the lake load provides a valuable constraint on viscosity variations within the crust and upper mantle (Bills et al., 1994).

The goal of my research is to improve models currently used to describe measurements of Lake Bonneville isostatic response. The approach includes augmenting Currey's (1982) shoreline elevation dataset measurements with denser sampling, including the addition of shorelines measured on the footwall of the Wasatch Fault. The new measurements are derived from a new cross-correlation and stacking approach described in Chapter 2, applied to modern GPS-RTK data and moder topographic DEMs. Ideally the additional data should decrease the influence of bias error on isostatic model parameters. In this chapter, I use algorithms developed for Generic Mapping Tools (GMT; Wessel and Smith, 2010) and Matlab (Mathworks®) to mathematically model a predicted isostatic response and compare it to the observed response to estimate parameters of flexural rigidity and viscosity. Models with and without the new measurements are compared to examine the impact of these data on model resolution.

Previous Work

Many previous researchers have used observations of Lake Bonneville shoreline elevations to estimate viscosity structure of the crust and upper mantle. G.K. Gilbert (1890) recognized the potential for elevation variations of Lake Bonneville shorelines to illuminate Earth processes as early as the late nineteenth century. In his 1890 work for the U.S. Geological Survey, he hypothesized the observed variations in shoreline elevation represented the response of a "...thin

solid crust resting upon a liquid substratum...(p. 379)", long before the more broadly-recognized work of Barrell (1914), Daly (1940), and Gunn (1943), and before Jeffreys (1924) convinced most of the U.S. Earth Science community that Wegener's (1915) theory of continental drift was falsifiable because mantle rock could not flow.

Crittenden (1963, 1967) modeled the Bonneville isostatic response as a 50 km thick elastic "crust" having a Young's Modulus (E) of 7×10^{11} Pa, and Poisson's ration (ν) of 0.25. The time-dependence of response was modeled to estimate a viscosity of the substrate of 10^{21} poises, or 10^{20} Pa s.

Many researchers have modeled isostatic rebound of Lake Bonneville following Gilbert's (1890) and Crittenden's (1963, 1967) pioneering efforts. Walcott (1970) reinterpreted data from Cittenden's (1963, 1967) earlier papers to estimate a "thickness of the lithosphere" for the Basin and Range province of little more than 20 km. Although he used a different terminology, this refers to T_e. Passey (1981) added 24 new measurements of Bonneville and Provo shoreline elevations to Crittenden's dataset. He estimated a viscosity of 2×10^{19} Pa s. Nakiboglu and Lambeck (1983) used the same shoreline observations to model both an elastic layer overlying a viscoelastic channel as well as an elastic layer overlying a viscoelastic half-space. They concluded that a 100 km thick channel would need a viscosity of $2.1\text{-}5.8 \times 10^{18}$ Pa s, and a thinner layer would require a much lower viscosity, whereas a half-space viscosity would be $1.5\text{-}3.4 \times 10^{19}$ Pa s. Bills and May (1987) used the same modeling approach as Nakiboglu and Lambeck (1983) for three lakeshore data sets instead of two (Bonneville, Provo, and Gilbert), using

shoreline uplift data collected by Currey (1982). The additional data yielded a 23 ±2 km T_e and a half-space viscosity of 1.2(±0.2)x10^{20} Pa s. Bills et al. (1994) used the Currey (1982) dataset to model linear viscosity as a function of depth beneath the basin. They applied forward and inverse modeling techniques, estimating T_e of around 20-25 km and depth-dependent mantle viscosities ranging from 2x10^{17} to 4x10^{20} Pa s. Although the flow driving the isostatic response is very likely to reflect a power-law (nonlinear) rheology, Bills and his colleagues were unable to distinguish uplift response driven by dislocation (power-law) creep from linear diffusion creep consistent with a Maxwell viscoelastic rheology, possibly due in part to the lack of internally consistent formulations describing stress-dependent viscoelastic flow.

The 20-25 km T_e estimate of Bills et al. (1994) differs significantly from the 5-15 km estimates for the eastern Basin and Range derived from geological-timescale isostatic balance reflected in gravity and topography (Bechtel et al., 1990; Lowry and Smith, 1994, 1995; Kirby and Swain, 2011; Lowry and Peréz-Gussinyé, 2011). This difference probably reflects the great difference in the timescale of loading and hence viscoelastic stress relaxation (e.g. Willet et al., 1985; Lowry and Smith, 1994). A long-term objective of the five-year National Science Foundation grant that funded this project is to reconcile these long-term and short-term estimates of T_e. This project takes the first few steps toward this goal by adding new measurement sampling of Bonneville shorelines, described more fully in Chapter 2 of this thesis, and examining their impact on estimates of isostatic parameters as described here.

Isostatic Modeling

I examine the impact of spatial sampling by modeling uplift response to lake unloading in two different ways. The first approach models the isosatic response of an elastic plate over an inviscid half-space. The second uses an elastic plate over a viscoelastic half-space, and incorporates the time-history of lake loading as well as unloading. I compare model predictions for each case with two data sets that have slightly different spatial sampling. The first data set is an isostatic uplift signal interpolated from shoreline elevations measured for each epoch (Bonneville, Provo, and Gilbert) by Currey (1982). The second includes 44 new measurements, derived with a cross-correlation and stacking algorithm described in Chapter 2, in addition to the Currey (1982) measurements.

To estimate the load in each case, shoreline elevation measurements were interpolated using a minimum curvature algorithm in Generic Mapping Tools (GMT; Wessel and Smith, 1998). The interpolated shoreline heights from Currey's (1982) data are depicted as uplift signals in Fig. 3.2b. I then subtracted a recent 30 arc-second resolution digital elevation model (DEM) provided by the USGS (GTOPO30, 2010) from the interpolated uplift file, resulting in positive values approximating the lake paleo-depth at each gridpoint within the lake area and negative values outside. I zeroed out all negative numbers as well as areas outside the lake basin with a lower elevation than Lake Bonneville, such as the Snake River Plain and the Bonneville outlet channel. The resulting map approximates lake paleo-depth corrected for the subsequent isostatic response (Fig. 2.1).

Elastic-Over-Inviscid Modeling of Currey Data Only

I next model the isostatic response to removal of the lake load for the case of an elastic layer over an inviscid half-space. For this I use a two-dimensional Fast Fourier Transform (FFT)-based algorithm, grdfft, in GMT that optionally calculates the isostatic flexural response to loading of an elastic plate over an inviscid half-space given a specified T_e. The algorithm assumes an input grid corresponding to height of a surface load with a crustal density of 2670 kg m^{-3}, so I multiply the lake depth by negative -1000 divided by 2670 to yield a rock "pseudo-height" with vertical stress equivalent to the lake load forcing term. The grdfft model of Bonneville unloading assuming T_e = 25 km is compared to the interpolated Currey (1982) measurements in Fig. 3.2.

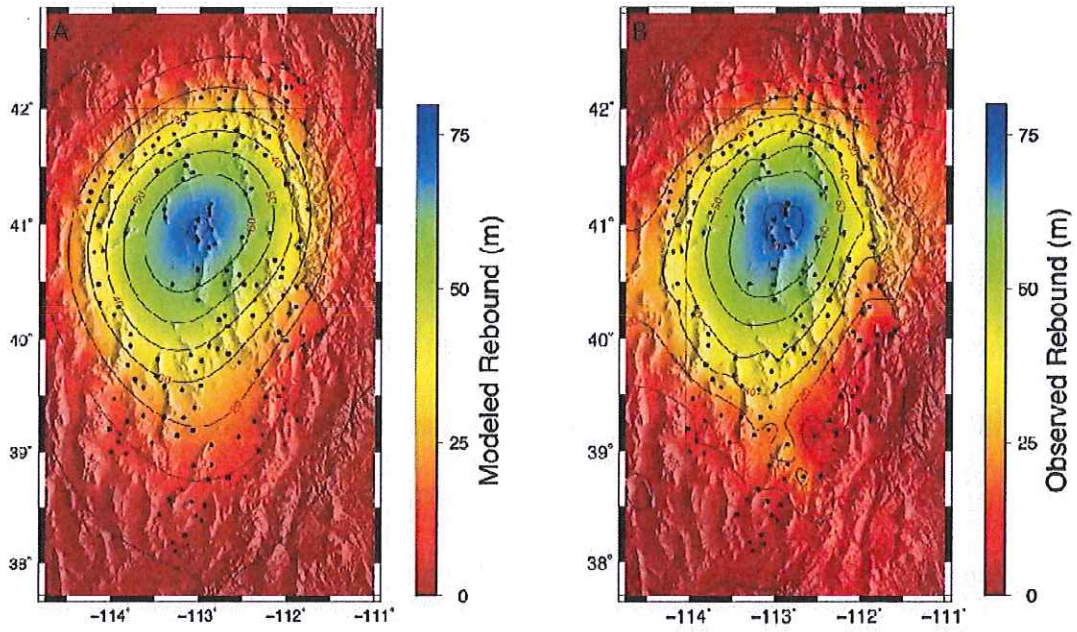

Figure 3.2: Best-fit predicted (A) and observed (B) uplift response for the Bonneville epoch, using an elastic layer over inviscid half-space model. Black dots represent locations of shoreline elevation measurements in Currey (1982).

The response is modeled for T_e from 1 to 70 km at 1-km interval, and the RMS misfit of the residual between the model prediction and interpolated measurements is calculated for each T_e (Fig. 3.3) to determine which T_e best fits the observed shoreline uplift.

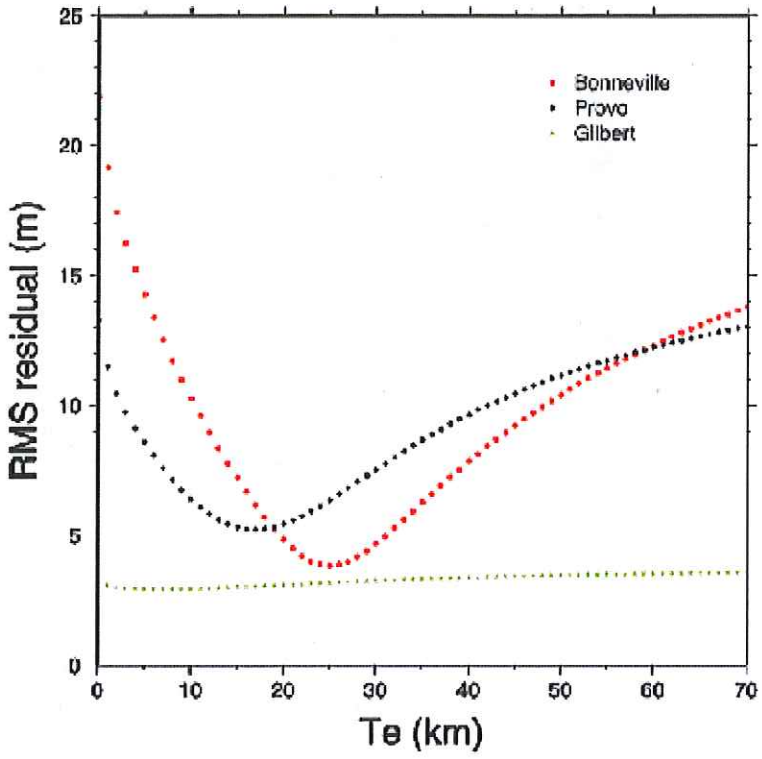

Figure 3.3: RMS misfit (in meters) between observed and modeled uplift versus T_e using only Currey's (1982) measurements of the Bonneville, Provo and Gilbert shorelines.

The residual of the best-fit model, corresponding to a T_e of 25±2 km, is shown in Fig. 3.4. The Provo and Gilbert shorelines were also modeled. The best-fit T_e for the Provo uplift is 17±km, and Gilbert level measurements are relatively insensitive to T_e, yielding a best-fit of 7 km and a 1σ confidence interval from 4 to 10 km.

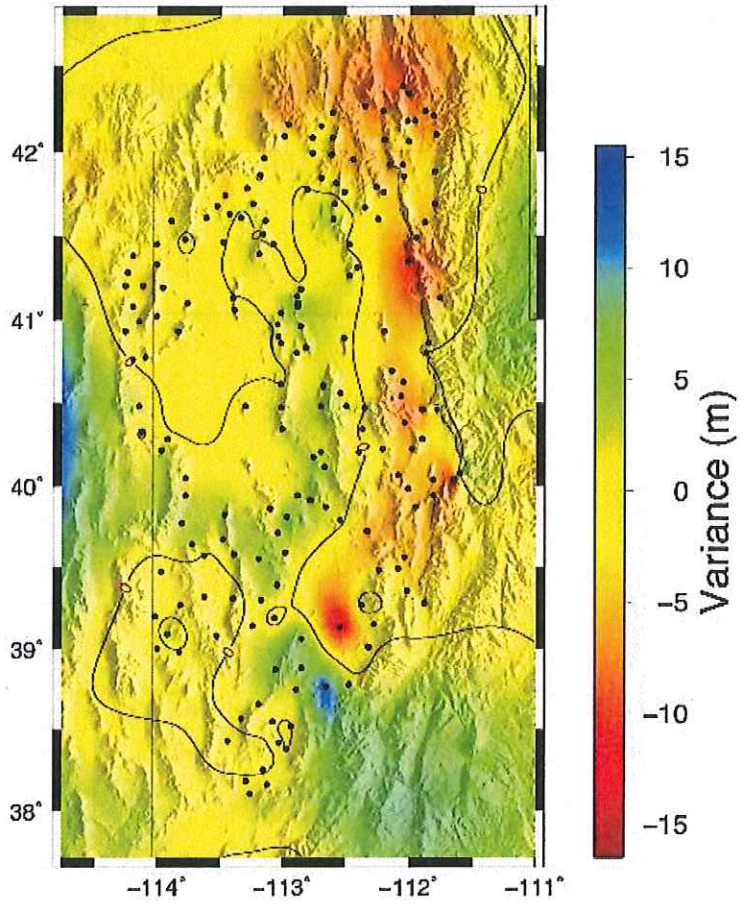

Figure 3.4: Misfit after subtracting the modeled response from the observed response of the Bonneville epoch from Currey's (1982) data.

This enables us to observe where the uplift either exceeds or is less than the predicted response and evaluate what other (unmodeled) processes may be responsible for the signal misfit.

Heights in the Currey (1982) dataset, used by Bills et al. (1987, 1994) and modeled in Figs. 3.3 and 3.4, were measured mostly from analyses of aerial photographs and topographic maps. Limitations inherent in these analyses include the errors introduced by interpolating from map contour intervals as much as 80 ft. In addition, Currey (1982) almost exclusively measured depositional shorelines

because it is much simpler to measure elevation of a depositional shoreline crest than it is to identify the knick-point of an erosional shoreline. Depositional features comprise only about 40% of the shoreline expression and occur primarily in locations of low relief, so (for example) only two shorelines were measured on the footwall of the Wasatch Fault, the most active fault in the region. Many of his data points are on the footwalls of other Basin and Range faults in the region, further west, and several measurements are on the hanging wall of the Wasatch, which may introduce a sampling bias to his dataset. Since fault displacements are not accounted for in isostatic models, this sampling distribution not only might contribute to the misfit, but the bias might also nudge the best-fit model parameterization away from the true values.

Augmentation of the Currey (1982) Data

I augmented Currey's (1982) shoreline elevation dataset with 44 measurements generated using the shoreline picking algorithm discussed in Chapter 2 and examine here the impacts of sample density and sampling bias on the model results. The additional measurements include 11 erosional shorelines located on the footwall of the Wasatch Fault, 12 erosional shorelines in other locations and an additional 21 depositional shorelines (see Appendix). I modeled the uplift with the additional erosional shorelines included to examine whether the bias error introduced into model parameters by neglecting erosional shoreline data was significant. First, I compared my measurements of both erosional and depositional shoreline heights to Currey's measurements at one location on

Antelope Island, to assess the potential for datum- or shoreline process-related bias introduced by adding shorelines to Currey's dataset.

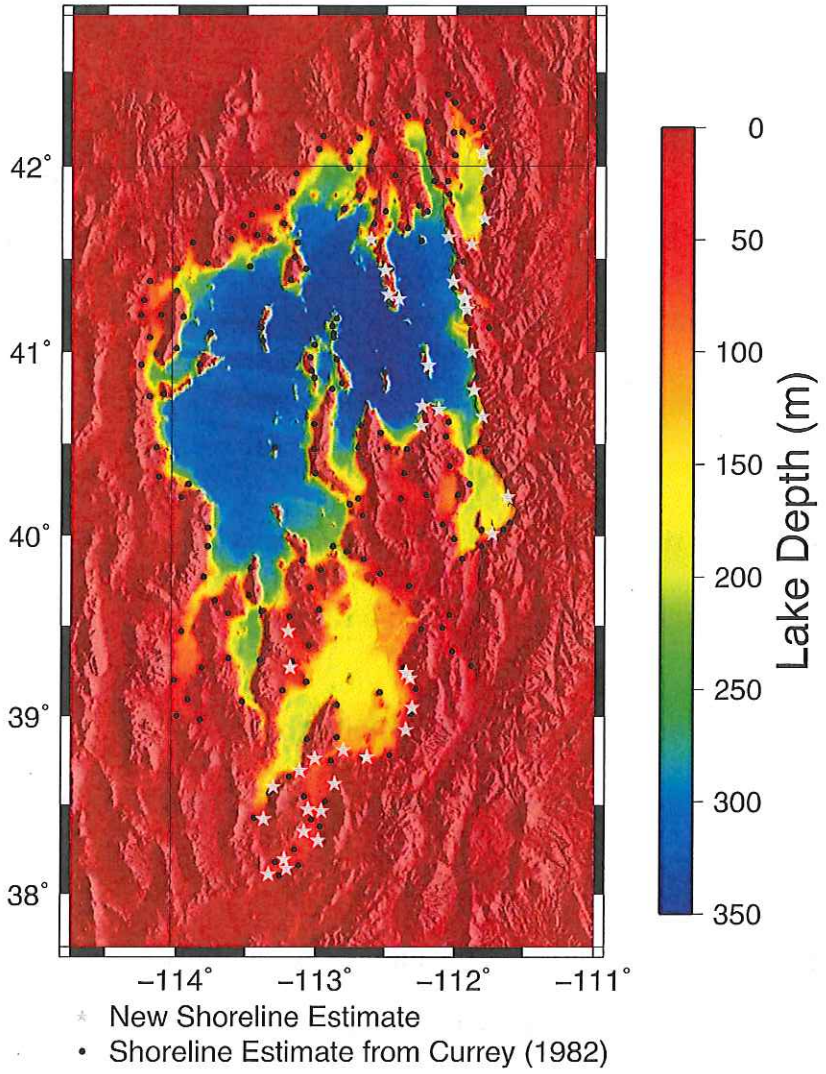

Figure 3.5: Lake Bonneville highstand paleo-depth estimates. Locations of Currey's (1982) measurements are indicated by small black dots; my additional estimates of shoreline elevation are shown as grey stars.

I identified a depositional shoreline near one of Currey's data points (i.e., within 1 km, the location uncertainty of Currey's published data) and I extracted a shoreline profile from a 2 m-sampled auto-correlated DEM. The data indicate a clearly identifiable "peak" with elevation 1598.7 m (Fig. 3.6).

This is well within uncertainty of Currey's (1982) measurement of 1599 +/- 2 m. I then extracted a profile of an erosional shoreline from the same 2 m-sampled DEM located ~240 m northeast of the depositional shoreline profile. This shoreline has a very distinctive knick-point that yields a strong peak in the curvature profile at 1604 m elevation (Fig. 3.7). Visual inspection of the shoreline suggests the knickpoint elevation is biased upward in the curvature by about 2m, consistent with the bias effect observed in tests of synthetic data as described in Chapter 2. Thus I assign an elevation of 1602 m to the knickpoint. Since this erosional shoreline is the baseline to which other erosional shorelines are compared to, this bias is accounted for in all estimates of shoreline elevation from erosional shorelines.

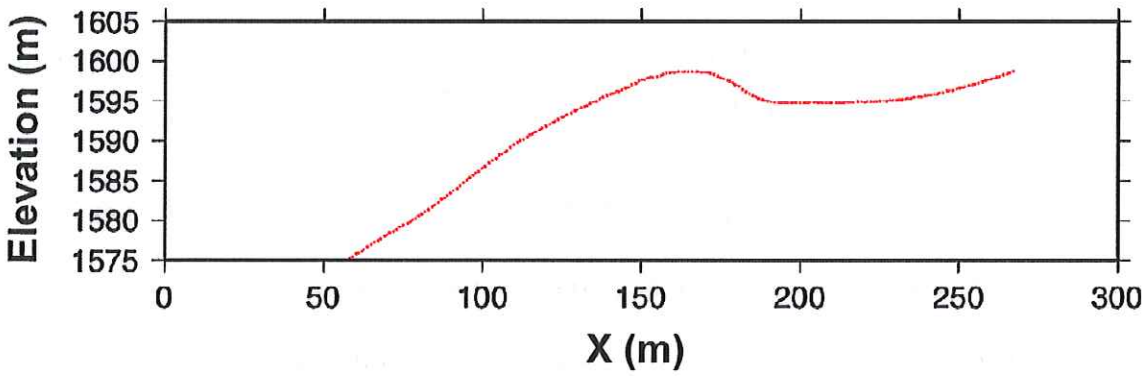

Figure 3.6: Profile of a barrier ridge on Antelope Island near where Currey (1982) measured a shoreline elevation of 1599 +/- 2m. The peak elevation on the barrier identified from this profile is 1598.7 m. Vertical Exaggeration is 5X.

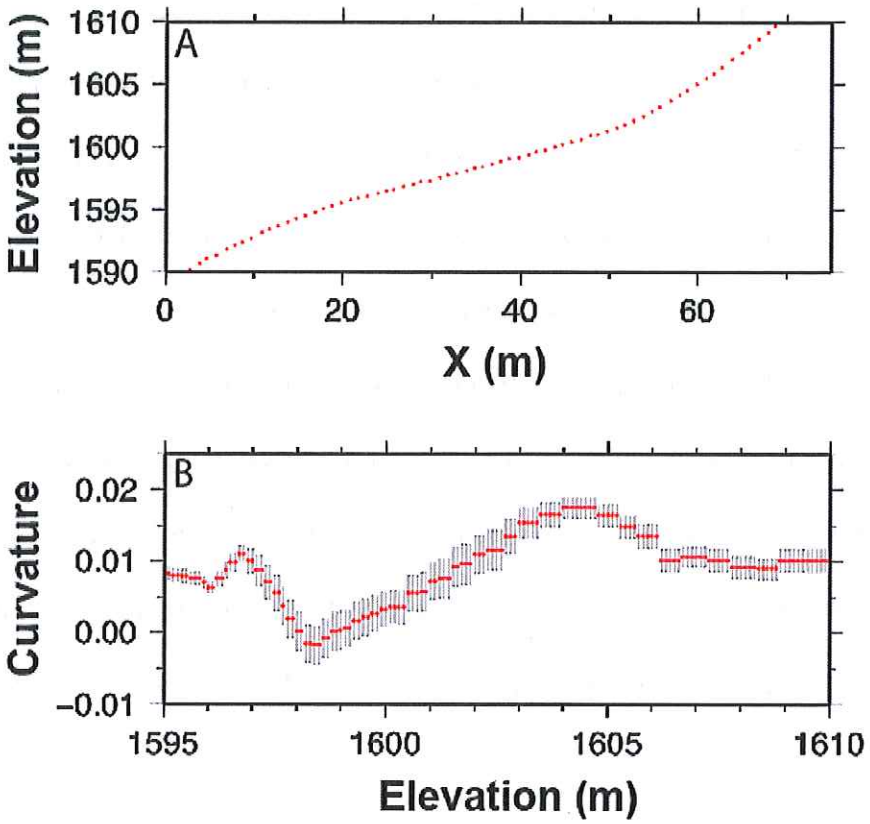

Figure (3.7): Profile (A) and curvature profile (B) of erosional shoreline on Antelope Island picked near point 29 from Currey (1982).

Since the knickpoint is the feature that most strongly influences estimates of correlation lag and elevation for the cross-correlation and stacking method described in Chapter 2, the approximately 3 m difference between depositional crest and erosional knickpoint heights would be problematic for comparisons of models and observations that use both erosional and depositional shorelines if it were a pervasive error. However, this discrepancy is not observed consistently on the ground when traversing from erosional to depositional shorelines. At least one field observation I made of a depositional shoreline that intersects an erosional shoreline found the depositional shoreline to sit clearly higher than the erosional

shoreline of the same age. The difference is likely related to the differences in processes and conditions responsible for forming the shoreline features on in each situation (Jack Oviatt, personal communication, 2011).

Elastic-Over-Inviscid Modeling of Augmented Data

RMS residuals of the modeled and observed uplift are shown in Fig. 3.8 for shoreline elevations estimated by Currey (1982) (Fig. 3.8a) and with additional measurements made for this study (Fig. 3.8b).

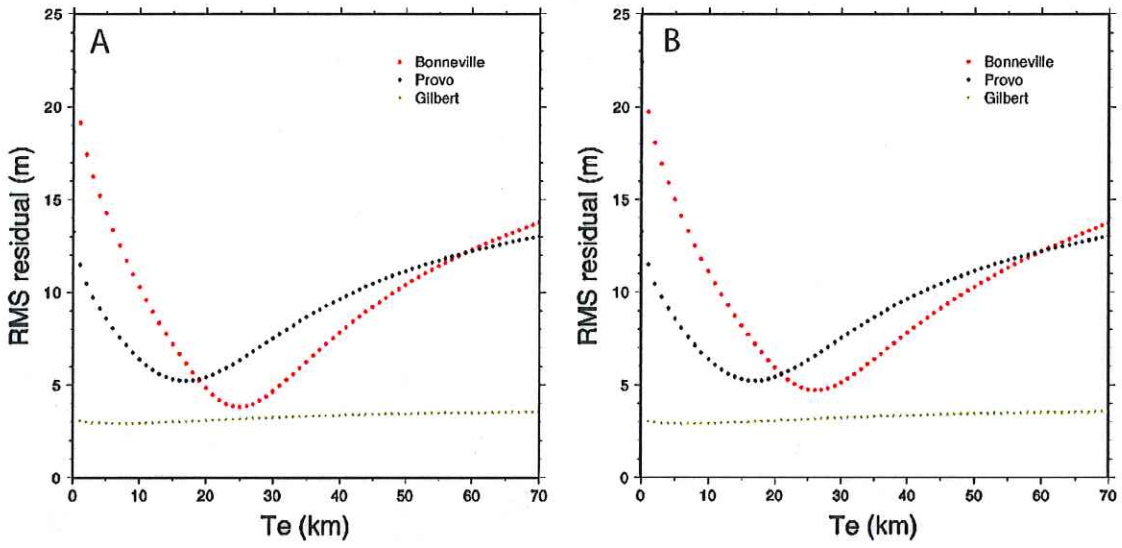

Figure 3.8: RMS misfit (in meters) of modeled and measured uplift as a function of T_e for (A) Currey's (1982) dataset and (B) the enhanced dataset described here.

The best fit for the Bonneville epoch occurs with a 25±2 km T_e and an RMS misfit of 3.8168 km when only Currey (1982) data are used. When compared to the observed response from the augmented dataset, the best fit for the Bonneville epoch occurs with a 26±2 km T_e and an RMS misfit of 4.7181 m. The greater misfit appears to be due mostly to the increased uplift signature along the Wasatch Fault, which

most likely reflects uplift on the footwall of the Wasatch Fault as a result of active faulting, but may also reflect a small bias introduced by the erosional shoreline.

Since I did measure additional shoreline heights for the Provo and Gilbert epochs, the misfits are unchanged for these epochs. The Provo epoch best fit occurs at a T_e of 17±3 km and an RMS misfit of 5.2298 m and the Gilbert epoch best fit occurs at a T_e of 7±3 km and an RMS misfit of 2.9305 m. We will discuss the relatively high misfit of the Provo epoch shortly. The relatively low misfit for the Gilbert is likely related to the small uplift observed for that epoch.

Observed uplift for the Currey-only and augmented datasets is distinctly different (Fig. 3.9). It is evident from Fig. 3.9c that additional shoreline measurements near the Wasatch Fault indicate footwall uplift that is not evident in Currey's (1982) data.

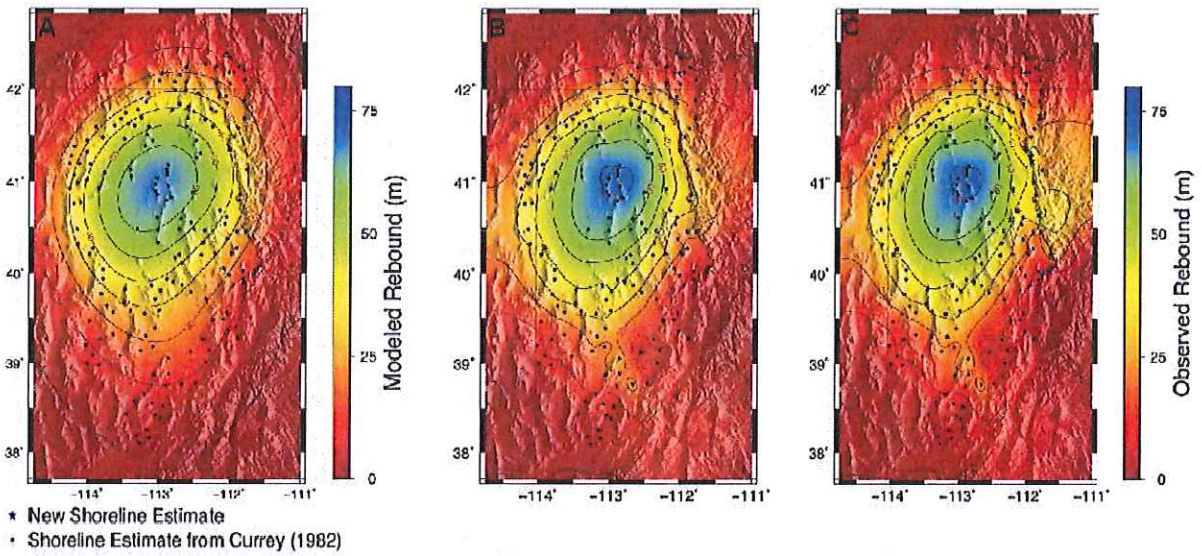

Figure 3.9: (A) Modeled uplift compared with observed isostatic response for (B) the Bonneville epoch using Currey's (1982) data and (C) with additional points measured using the cross-correlation algorithm described in Chapter 2.

The RMS misfit associated with this tectonic signal likely is amplified by the comparison of interpolated grids, as the interpolation extends that uplift signal to distances of up to 100 km east of the measurements. This signal is more readily seen in residual height variations, after subtracting a best-fit isostatic model, as depicted in Fig. 3.10.

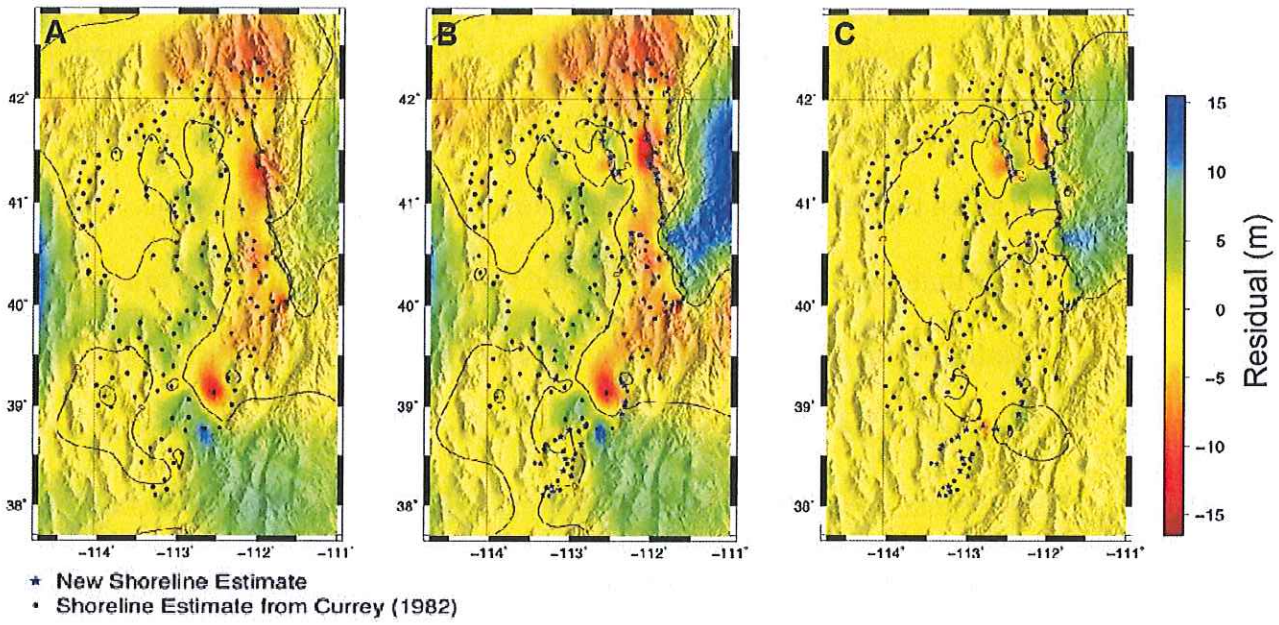

Figure 3.10: RMS variance between the modeled response and the observed response for (A) observed response using only Currey's (1982) data, (B) observed response using the enhanced dataset and (C) difference between the two residuals.

Figure 3.10c clearly shows that the majority of the difference is an uplift signal from shorelines taken along the Wasatch Fault, and to a smaller degree, the East Cache Fault. Some of this uplift may represent a bias introduced by shift of the knickpoint elevation introduced in the curvature calculation, and it may also reflect differences in the shoreline processes that create the knickpoint as described in Chapter 2. However, many of the erosional shorelines added to the data set exhibit

little or no change from the interpolations of Currey's results, and some show a slight decrease in elevation. Hence I conclude based on these observations that the bias introduced by adding erosional shorelines to a predominantly depositional shoreline dataset is negligible.

Elastic-Over-Viscoelastic Model

I use forward modeling techniques to solve for a best-fit T_e and viscosity (η) by modeling the Bonneville and Provo shoreline uplift expected for a range of T_e and η given the current knowledge of lake level changes through time. The lake depth files that were calculated in GMT and used to create figures 1.1 are imported into Matlab® and a load is calculated at a 1 km grid spacing. The shoreline elevation dataset is also imported into Matlab® from which the observed uplift signal is interpolated over the region of interest. A simple load history is constructed assuming linear loading from 34 ka to the Bonneville level at 17.8 ka followed by a rapid unloading to Provo level at 17.4 ka and a cessation of the Provo level at 14.4 ka (the approximate midtime of lake regression from 15.2 to 13.5 ka). This history is described in more detail in Chapter 2. The flexural rigidity, D, relates to effective elastic thickness as (Turcotte and Schubert, 2007):

$$D = \frac{T_e^3 E}{12(1-\nu^2)} \qquad \text{(Equation 3.1)}$$

The elastic parameters used for modeling were calculated from a weighted average of geophysical properties in Crust 2.0 (Bassin et al., 2000). Within the Bonneville basin, the average lithospheric Young's modulus E=1.309x10^{11} and the average

lithospheric Poisson's ratio ν=0.2613 with a crustal thickness of 31 km. The Load is Fourier transformed into the wavenumber domain and then applied into the following equation (Turcotte and Schubert, 2007):

$$w(t) = \int_{34\,ka}^{t} L(k,\tau)\frac{1-\exp\left(\frac{-\rho_m g\tau}{2k\eta}\right)}{\Delta\rho + \frac{D}{g}k^4}d\tau \qquad \text{(Equation 3.2)}$$

where w is vertical displacement, $L(k)$ is the two-dimensional Fourier transform of the load, ρ_m is the density of the mantle, $\Delta\rho$ is the difference in density between the top and bottom of the lithosphere and k is the wavenumber. I evaluated the integral numerically at times corresponding to the end of Bonneville loading, the end of Provo loading and the present, and modeled the observed shoreline deflection as differences in w across these timespans. These displacements Δw for each combination of T_e and η are compared with the observed response interpolated from the shoreline elevation dataset and the RMS of the misfit at the measurement locations, weighted by inverse variance of the measurement to give a WRMS, is calculated to determine the best-fit parameterization.

The viscoelastic models are compared first to Currey (1982) data only, and then to the augmented data. With Currey (1982) data only, the best-fit occurs at a T_e of 70±5 km and viscosity has best-fit ~2×10^{18} Pa s and ranges from ~1×10^{18} Pa s to ~5×10^{19} Pa s at 95% confidence, with an RMS of 15.6568 m. With the augmented data, the best-fit occurs at a T_e of 58±2 km and a viscosity ranging from 1×10^{18} Pa s to 1×10^{19} Pa s at 95% confidence and an RMS of 12.1269 m (Fig. 3.11).

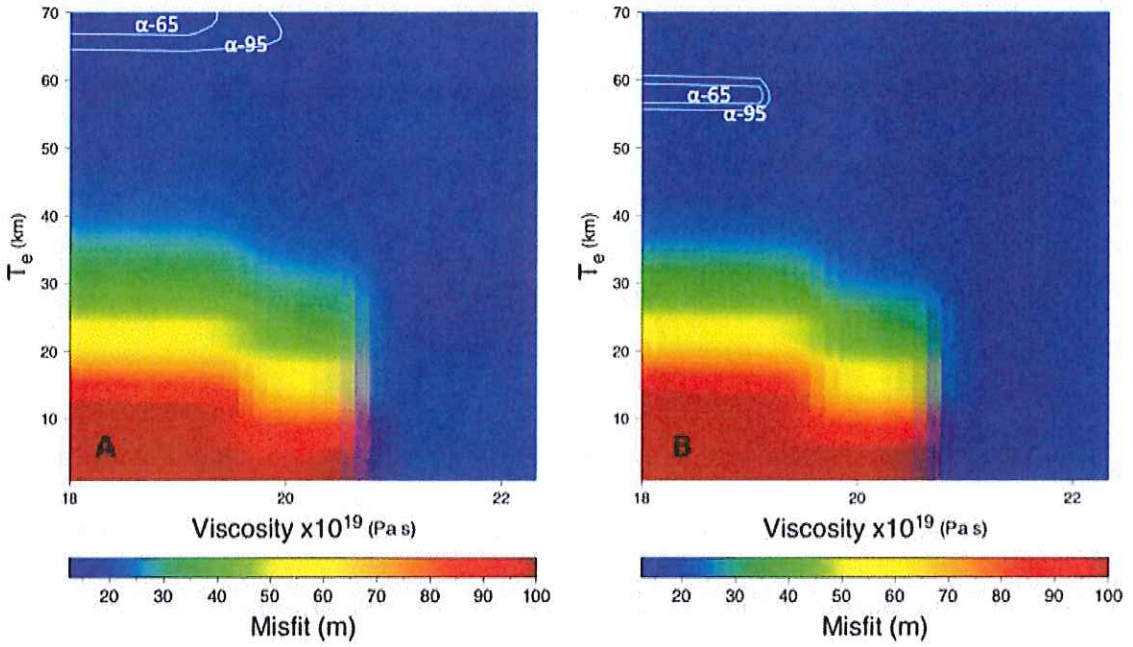

Figure 3.11: RMS misfit of T_e and viscosity pairs for (A) Currey (1982) only data and (B) the augmented data. Confidence intervals depicted at 65% and 95%.

Comparisons of uplift at each sampled point for the model and the observed case are depicted in Fig. 3.12 for the Bonneville level and Fig. 3.13 for the Provo level. In Fig. 3.11, the augmented dataset yields a T_e and viscosity closer to expected values and at lower WRMS misfit that does the Currey (1982) only dataset. The T_e for both cases is still much higher than predicted and varies greatly from models by previous researchers. Differences in the methods used here can explain the differences such as size and shape of load pixels [e.g. 1km square pixels used here vs. circles with 25 mile radius used by Crittenden (1967)] as well as increased sampling. What is likely the greatest discrepancy between the models is the load history, which has been refined since the last modeling attempts. The best-known Provo occupation has increased in duration from around 500 years, as modeled by

Bills et al. (1994), to over 2000 years from improved resolution on the Carbon dating timescale and improved sampling techniques (Godsey et al., 2011).

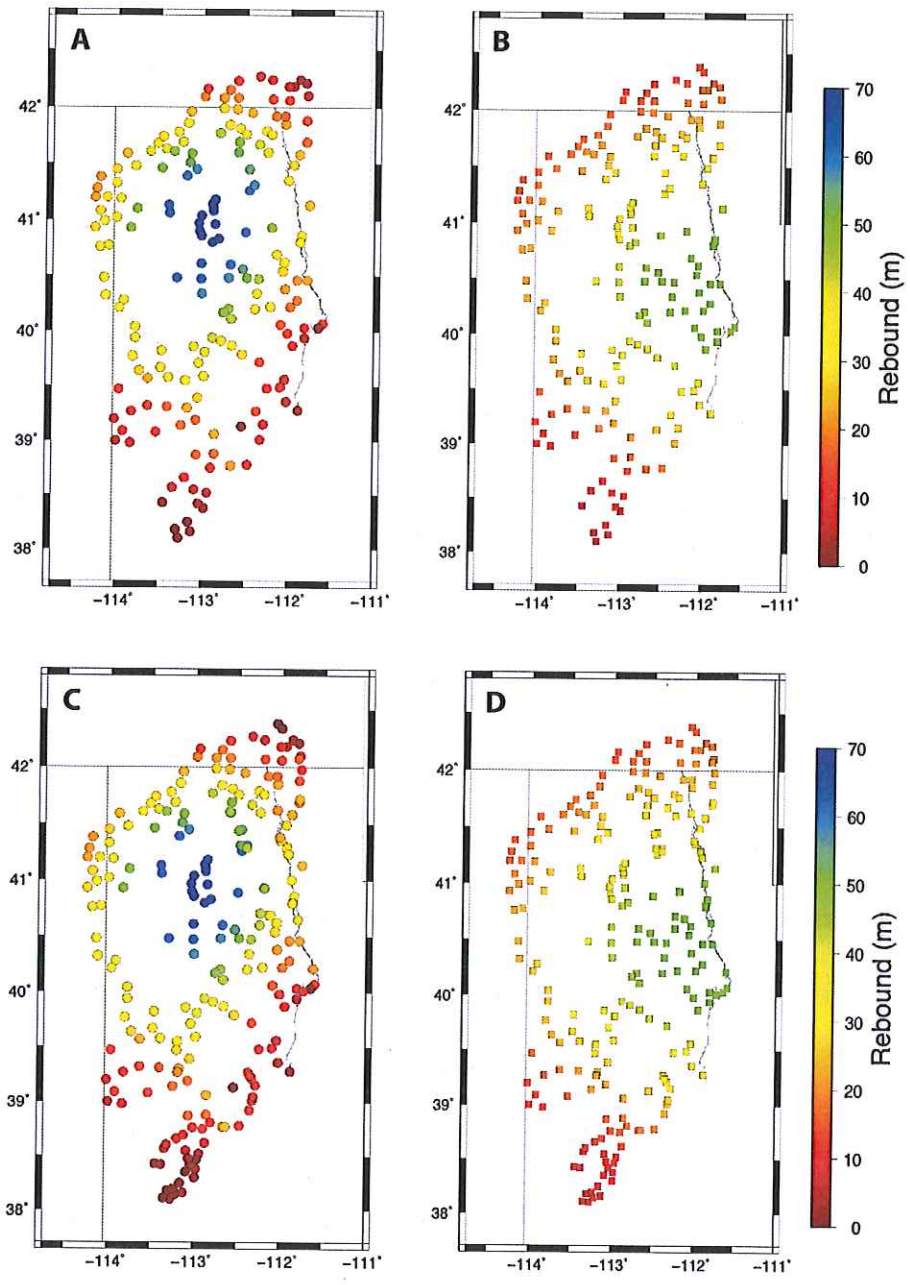

Figure 3.12: Point map of Bonneville level sampling locations comparing (A) observed response from Currey (1982) data only; (B) modeled response from Currey (1982) data only; (C) observed response from augmented data and (C) modeled response from augmented data.

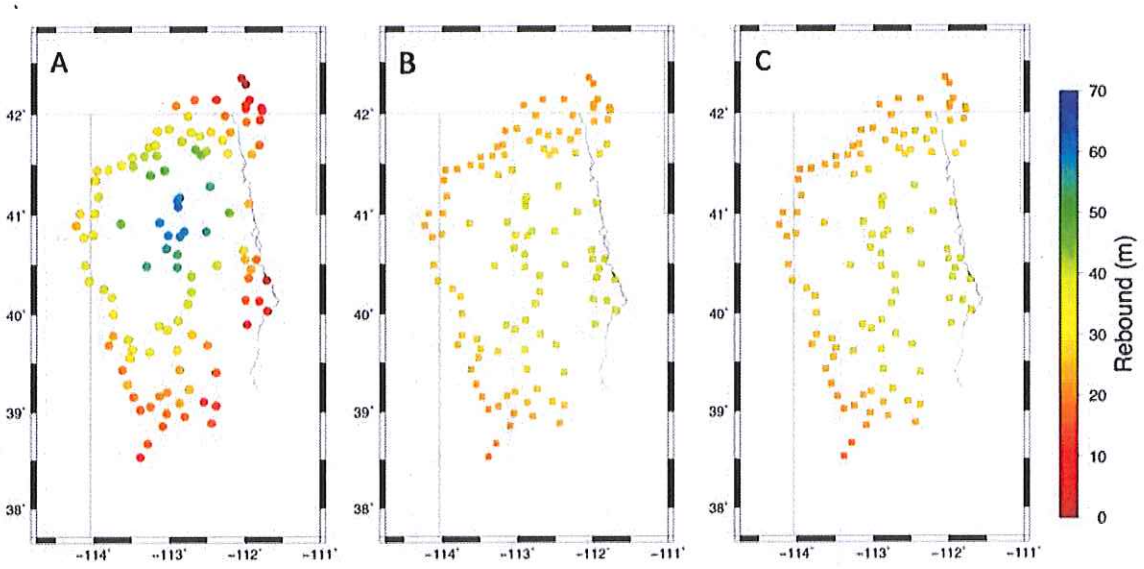

Figure 3.13: Point map of Bonneville level sampling locations comparing (A) observed response from Currey (1982) data only; (B) modeled response from Currey (1982) data only; (C) modeled response from augmented data.

In Fig. 3.12 it is apparent that the modeled displacement is greatest to the east of the observed greatest displacement. The model seems to actually place the greatest displacement near the Wasatch Fault, which is where we actually observe subsidence. This is likely the reason for the lower WRMS using the augmented data since it accounts for the uplift on the footwall side of the fault. The Wasatch Fault zone is the east boundary of the Basin and Range province with the Rocky Mountain province on the footwall side. The shifted focus of displacement that is observed possibly results as a very different set of parameters exists for the footwall side of the fault than for the hanging wall side of the fault. Since the hanging wall side is weaker, the displacement was possibly focused there rather than where the model,

which assumes uniform properties for the entire region, predicts the maximum displacement would take place.

Discussion

The models generated with new shoreline elevations measured on the footwall of the Wasatch Fault clearly show a significant uplift signal, which coordinates with the subsidence evident on the hanging wall side. The additional elevations from the Weber, Salt Lake, and Provo segments seem to all demonstrate markedly increased positive variance along these segments indicating an increased uplift signal. This result is expected. However, the elevations taken from the Brigham City segment do not show any uplift as predicted. In fact they have the opposite trend. Probably the easiest explanation is that I picked a location in which the fault actually crosses to the east of the Bonneville level shoreline, which would result in a subsidence signal instead of an uplift signal. Another possible explanation could be the paleoseismic trend. The Brigham City segment has not ruptured in more than 2,000 years (McCalpin and Nishenko, 1996), making it the least recent segment to rupture. Using this explanation it is still difficult to explain the subsidence trend that seems pervasive along this segment. This segment has ruptured at least 7 times since unloading of Lake Bonneville (McCalpin and Nishenko, 1996), so a significant signal is still expected. The southern part of the Brigham City segment even shows evidence for a surface rupturing event as recently as 1.1-1.3 ka (DuRoss et al., 2010) possibly resulting from spillover from the Weber segment rupture that occurred around the same time. From Hetzel and Hampel

(2005) subdued activity on the Wasatch Fault as the lake load persisted could have resulted in an accelerated displacement rate following unloading, which could produce up to 6-7 meters of displacement on average along the Wasatch Fault rather than the roughly 2.5 m expected from current displacement rates (figure 3.14).

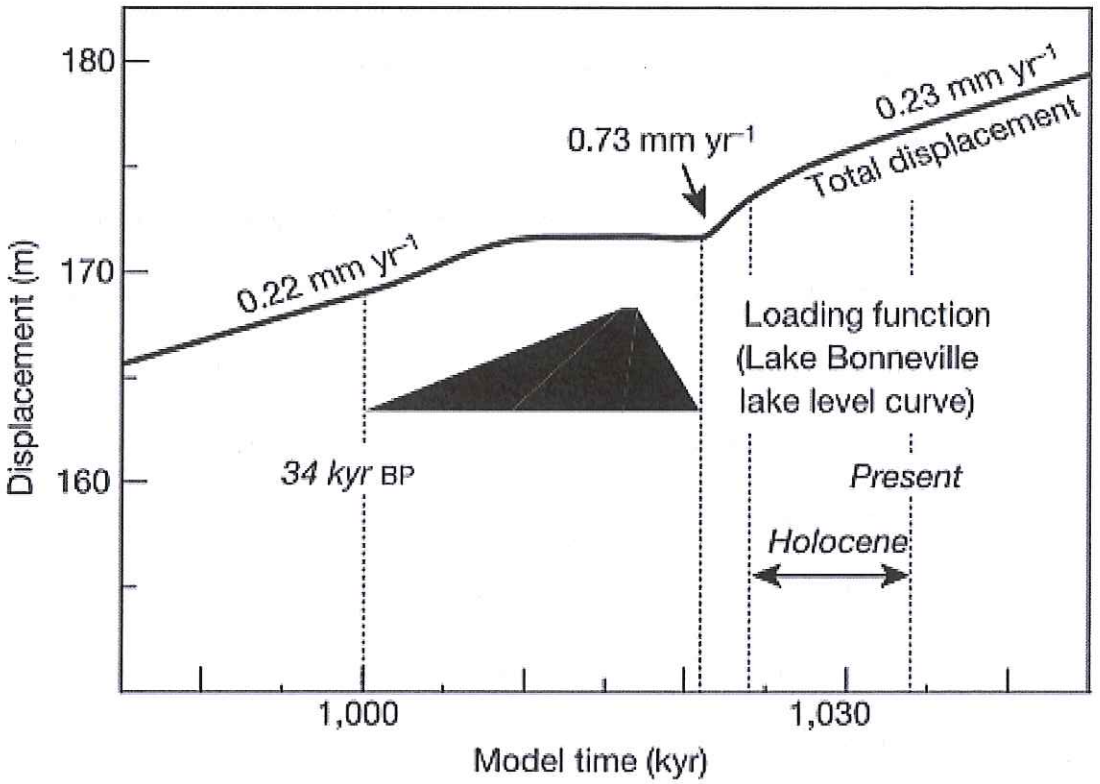

Figure 3.14: This model by Hetzel and Hampel, 2005, could account for up to 6-7 m of displacement on the Wasatch Fault since the load was removed.

Another explanation could be the proximity to the Snake River Plain. The persistent load of dense volcanic rock in the Snake River Plain is likely still producing subsidence in the surrounding regions, which provides a probable explanation for the strong subsidence throughout the northern Bonneville basin,

evident in misfit maps for the Provo level as well, and could possibly subdue the signal of uplift from the fault so that it is not readily distinguishable from the subsidence. More effort will be necessary to resolve this discrepancy.

Conclusion

The addition of shoreline elevation estimates on the footwall of the Wasatch Fault create a more complete model of processes that are interfering with the Bonneville isostatic response signal in the form of subsidence along the hanging wall near the fault zone and uplift along the foot wall near the fault zone. In order to reconcile viscosity using the variation between the Bonneville and Provo stage responses, the Wasatch Fault signal (and likely signals from other fault systems in the basin) as well as the anomalous uplift in the south part of the basin and the subsidence in the north part of the valley will need to be resolved in order to compensate for these signals in the model. In addition, future attempts at modeling the isostatic uplift would be wise to take into account the abrupt shift in parameters that likely occurs between the Basin and Range to the west of the Wasatch Fault and the Rocky Mountain province to the East. The shoreline elevation estimation method presented in Chapter 2 lays the foundation for obtaining additional data. In this chapter, the usefulness of this data is presented in helping to quantify the signals that are interfering with more accurate modeling of isostasy.

References

Bard, E., B. Hamelin, R.G. Fairbanks, and A. Zindler, Calibration of the ^{14}C timescale of the past 30,000 years using mass spectrometric U-Th ages from Barbados corals, *Nature, 345*, 405-410, 1990.

Barrel, J., The strength of the Earth's crust, *J. Geol., 22 (4),* 289-314, 1914.

Bassin, C., G. Laske, and G. Masters, The current limits of resolution for surface wave tomography in North America, *EOS, 81*, F897, 2000.

Bechtel, T.D., D.W. Forsyth, V.L. Sharpton, and R.A.F. Grieve, Variations in effective elastic thickness of the North American lithosphere, *Nature, 343,* 636-638, 1990.

Benson, L.V., S.P. Lund, J.P. Smoot, D.E. Rhode, R.J. Spencer, K.L. Verosub, L.A. Louderback, C.A. Johnson, R.O. Rye, and R.M. Negrini, The rise and fall of Lake Bonneville between 45 and 10.5 ka, *Quat. Intern., 235*, 57-69, 2011.

Bills, B.G., D.R. Currey, and G.A. Marshall, Viscosity estimates for the crust and upper mantle from patterns of lacustrine shoreline deformation in the Eastern Great Basin, *J. Geophys. Res., 99*, 22,059-22,086, 1994.

Bills, B.G., and G.M. May, Lake Bonneville: Constraints on lithospheric thickness and upper mantle viscosity from isostatic warping of Bonneville, Provo, and Gilbert stage shorelines, *J. Geophys. Res., 92*, 11,493-11,508, 1987.

Currey, D.R., Lake Bonneville: Selected features of relevance to neotectonic analysis, *U.S. Geol. Surv. Open-File Rep., 82-1070*, 31 pp., 1982.

Crittenden, M.D., Jr., Effective viscosity of the Earth derived from isostatic loading of Pleistocene Lake Bonneville, *J. Geophys. Res., 68*, 5517-5530, 1963.

Crittenden, M.D., Jr., Viscosity and finite strength of the mantle as determined from water and ice loads, *Geophys. J. R. Astron. Soc., 14*, 261-279, 1967.

Daly, R.A., *Strength and Structure of the Earth*, 434 pp., Prentice Hall, Princeton, N.J., 1940.

DuRoss, C.B., S.F. Personius, A.J. Crone, G.N. McDonald, and R.W. Briggs, Late Holocene earthquake history of the Brigham City segment of the Wasatch Fault Zone at the Hansen Canyon, Kotter Canyon, and Pearsons Canyon trench sites, Box Elder County, Utah, *U.S. Geol. Surv. Ext. Grant Awd. Num. 08HQGR0082*, 66 pp., 2010.

Gilbert, G.K., Lake Bonneville, *U.S. Geol. Surv. Monogr., 1*, 438 pp., 1890.

Godsey, H.S., C.G.Oviatt, D.M. Miller, and M.A. Chan, Stratigraphy and chronology of offshore to nearshore deposits associated with the Provo shoreline, Pleistocene Lake Bonneville, Utah, *Palaeogeogr. Palaeoclimatol. Palaeoecol., 310*, 442-450, 2011.

GTOPO30, http://www1.gsi.go.jp/geowww/globalmap-gsi/gtopo30/gtopo30.html. accessed 2010-2012.

Gunn, R., A quantitative evaluation of the influence of the lithosphere on the anomalies of gravity, *J. Frank. Inst., 236*, 47-66, 1943.

Hetzel, R., and A. Hampel, Slip rate variations on normal faults during glacial-interglacial changes in surface loads, *Nature, 435*, 81-84, 2005.

Janecke, S.U., and R.Q. Oaks Jr., New insights into the outlet conditions of late Pleistocene Lake Bonneville, southeastern Idaho, USA, *Geosphere, 7*, 1369-1391, 2011.

Jeffreys, H., *The Earth, It's Origin, History, and Physical Constitution*, 278 pp., University Press, Cambridge, 1924.

Kirby, J.F., and C.J. Swain, Improving the spatial resolution of effective elastic thickness estimation with the fan wavelet transform, *Computers Geosciences, 37,* 1345-1354, 2011.

Lowry, A.R., and M. Pérez-Gussinyé, The role of crustal quartz in controlling Cordilleran deformation, *Nature, 471*, 353-357, 2011.

Lowry, A.R., and R.B. Smith, Strength and rheology of the western U.S. Cordillera, *J. Geophys. Res., 100, 1*7,947-17,963, 1995.

Lowry, A.R., and R.B. Smith, Flexural rigidity of the Basin and Range-Colorado Plateau-Rocky Mountain transition from coherence analysis of gravity and topography, *J. Geophys. Res., 99*, 20,123-20,140, 1994.

McCalpin, J.P., and S.P. Nishenko, Holocene paleoseismicity, temporal clustering, and probabilities of future large (M>7) earthquakes on the Wasatch fault zone, Utah, *J. Geophys. Res., 101*, 6233-6253, 1996.

Nakiboglu, S.M., and K. Lambeck, A reevaluation of the isostatic rebound of Lake Bonneville, *J. Geophys. Res., 88*, 10,439-10,447, 1983.

Passey, Q.R., Upper mantle viscosity derived from the difference in rebound of the Provo and Bonneville shorelines: Lake Bonneville Basin, Utah, *J. Geophys. Res., 86*, 11,701-11,708, 1981.

Schofield, I., P. Jewell, M. Chan, D. Currey, and M. Gregory, Shoreline development, longshore transport and surface wave dynamics, Pleistocene Lake Bonneville, Utah, *Earth Surf. Proc. Landforms, 29*, 1675-1690, 2004.

Turcotte, D.L., and G. Schubert, *Geodynamics, 2nd Edition*, 456 pp., Cambridge University Press, New York, 2007.

Walcott, R.I., Flexural rigidity, thickness, and viscosity of the lithosphere, *J. Geophys. Res., 75,* 3941-3954, 1970.

Wegener, A., *Die Entstehung der Kontinente und Ozeane*, 146 pp., Braunschweig, Germany, 1915.

Wessel, P. and W.H.F. Smith, Generic Mapping Tools, http://gmt.soest.hawaii.edu/, accessed 2010-2012.

Willet, S.D., D.S. Chapman, and H.J. Neugebauer, A thermo-mechanical model of continental lithosphere, *Nature, 314*, 520-523, 1985.

CHAPTER 4

SUMMARY AND DISCUSSION OF IMPLICATIONS

Summary of Results

Here I have developed a cross-correlation approach to identifying differences in elevation between shoreline topographic breaks. Using this algorithm, a denser sampling of shorelines for Lake Bonneville was calculated and applied towards modeling flow parameters responsible for observed isostatic uplift in response to removal of the water load. I first compare observed uplift and the modeled response to unloading of an elastic plate over an inviscid asthenosphere as a function of assumed effective elastic thickness (T_e). The best-fit T_e for the Bonneville uplift is 25±2 km using only shoreline elevation estimates compiled previously and 26±2 km when these are augmented with 44 new measurements. No new measurements are collected for subsequent lake levels, but the best-fit T_e for the Provo uplift is 17±3 km, and Gilbert level measurements are relatively insensitive to T_e. I then model shoreline uplift in response to the entire history of loading and unloading, assuming an elastic plate over an isoviscous viscoelastic asthenosphere. This approach assumes parameters remain unchanged throughout the loading history, and yields a best-fit model with T_e=70±5 km and viscosity η=~2x10^{18} Pa s with 95% confidence ranging from ~1x10^{18} Pa s to ~5x10^{19} Pa s when only prior measurements are used. With the newer data added, the best-fit model has T_e=58±2 km and η ranging from ~1x10^{18} Pa s to ~1x10^{19} Pa s with 95% confidence.

Implications of T_e Results

After Crittenden's (1967) work, most workers characterized the apparent strength of the lithosphere by the flexural rigidity (D), which is commonly expressed as an equivalent effective elastic thickness (T_e) (Walcott, 1970). In continental lithosphere, T_e has no simple relation to any particular depth, but rather can be thought of as an imaginary elastic plate that has identical bending strength and isostatic response properties as the lithosphere (Burov and Diament, 1995; Lowry and Smith, 1995). This is a more illuminating way to conceptualize the mechanical strength of the lithosphere. However, it sows confusion as well: relatively few Earth scientists are aware that flexural rigidity can be directly related to the rheological properties that govern dynamical flow strength of the lithosphere on geological timescales.

Laboratory studies of rock flow at high temperatures and pressure suggest that continental crustal minerals flow at lower temperatures than those in the mantle (e.g., Bürgmann and Dresen, 2008). Consequently some researchers have suggested a possible decoupling of stronger crustal and mantle layers across a more fluid lower crust (Smith and Bruhn, 1984; Burov and Diament, 1996; Brown and Phillips, 2000). This possibility is illuminated by examining yield strength envelopes (YSEs; e.g., Goetze and Evans, 1979) which clearly show quartz, a major building block of the crust, to be much weaker than olivine at temperatures found in the lower crust (Fig. 3.2).

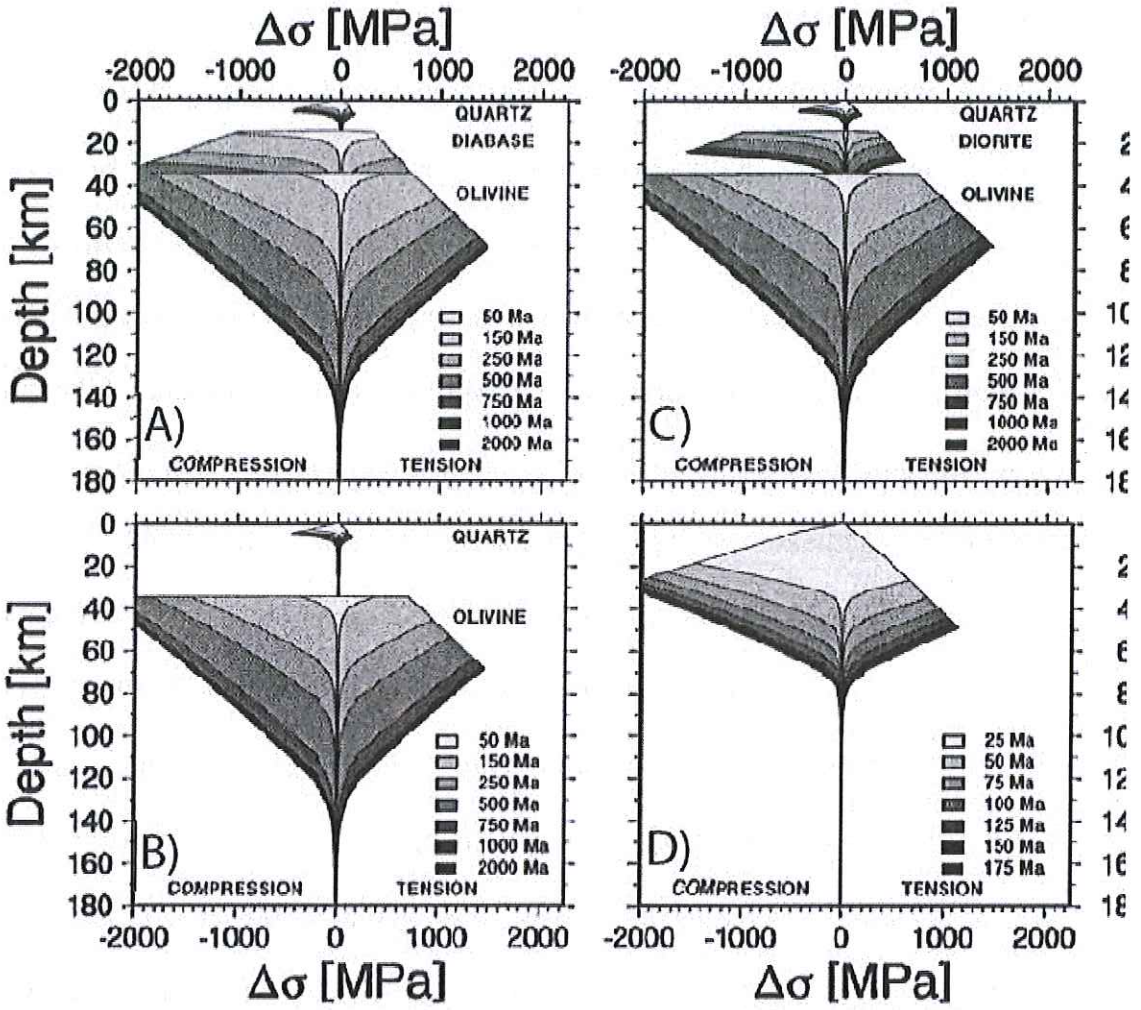

Figure 4.1: After Fig. 3a of Burov and Diament (1995). Yield-strength envelopes (YSEs) for continental lithosphere with different geotherms (expressed as "ages") and compositions of the lower crust: A, high-temperature of creep activation (diabase); B, low temperature of creep activation (quartzites, granites); C, intermediate temperature of creep activation (quartz-diorite). D corresponds to oceanic lithosphere. The upper (linear) parts of the YSEs are stress limits for brittle failure, the lower parts (decreasing with depth) represent limits for failure in ductile creep. The figure shows the crust is almost always decoupled from the mantle for a high geothermal gradient (<250 Ma "age"). For old lithosphere (>750 Ma "age") the crust and mantle may behave as a welded unit.

Because of the high dependence of the YSE on temperature, younger continental crust with a relatively high geothermal gradient can flex independently of the mantle because of flow at the base. However colder crust will likely be

welded to the mantle. Lowry and Peréz-Gussinyé (2011) observed a correlation of crustal quartz abundance to deforming zones and hypothesized that the weakness of quartz relative to other minerals exerts a primary control on lithospheric-scale deformation. When combined with the laboratory measurement-derived YSEs for quartz and olivine and measurements of low T_e in deforming regions, this strongly supports flow decoupling in warm continental lithosphere. Decoupled lithosphere favors lower T_e, but it is not always recognizable from flexural strength alone (Burov and Diament, 1996; Brown and Phillips, 2000). In addition to temperature and composition of the lithosphere, T_e is a function of time since loading, decreasing over time as stresses relax (Willet et al., 1985).

I model a T_e of 25±2 km with Currey (1982) data only for the Bonneville level assuming an elastic plate over an inviscid half-space. With the augmented data, the result is 26±2 km. This result is consistent with that of Bills et al. (1994), however, with Provo level data (Currey, 1982) I model a T_e of 17±3 km, which is significantly lower. This indicates the inadequacy of the elastic plate over a fluid substrate model and the necessity of a load history-dependent viscoelastic model. With this type of model applied to a simplistic load history, Currey's (1982) data estimates a T_e of 70±5 km with η=~2x10^{18} Pa s, but ranging from ~1x10^{18} to ~5x10^{19} Pa s. With the augmented dataset, the result is a little closer to previously modeled results with a T_e of 58±2 km and η ranging from ~1x10^{18} to ~1x10^{19} Pa s. With the vast differences experience here in relation to results from previous researchers, it is evident that this method will require further testing and refining to ascertain its validity. The methodology for estimating shoreline elevations and modeling

techniques described in this thesis, the groundwork is established for future researches to substantially increase the sampling of shoreline elevation data for Lake Bonneville, and the modeling techniques described can be refined to more accurately estimate lithospheric flow parameters with the aid of an increased sampling.

References

Bills, B.G., D.R. Currey, and G.A. Marshall, Viscosity estimates for the crust and upper mantle from patterns of lacustrine shoreline deformation in the Eastern Great Basin, *J. Geophys. Res., 99*, pp. 22,059-22,086, 1994.

Brown, C.D., and R.J. Phillips, Crust-mantle decoupling by flexure of continental lithosphere, *J. Geophys. Res., 105*, 13,221-13,237, 2000.

Bürgmann, R., and G. Dresen, Rheology of the lower crust and upper mantle: Evidence from rock mechanics, geodesy and field observations, *Ann. Rev. Earth Plan. Sci., 36,* 531-567, 2008.

Burov, E., and M. Diament, The effective elastic thickness (T_e) of continental lithosphere: What does it really mean?, *J. Geophys. Res., 100*, 3905-3927, 1995.

Burov, E., and M. Diament, Isostasy, equivalent elastic thickness, and inelastic rheology of continents and oceans, *Geol., 24*, 419-422, 1996.

Currey, D.R., Lake Bonneville: Selected features of relevance to neotectonic analysis, *U.S. Geol. Surv. Open-File Rep., 82-1070*, 31 pp., 1982.

Goetze, C., and B. Evans, Stress and temperature in the bending lithosphere as constrained by experimental rock mechanics, *Geophys. J. R. Astron. Soc., 59*, 463-478, 1979.

Lowry, A.R., and M. Pérez-Gussinyé, The role of crustal quartz in controlling Cordilleran deformation, *Nature, 471*, 353-357, 2011.

Lowry, A.R., and R.B. Smith, Strength and rheology of the western U.S. Cordillera, *J. Geophys. Res., 100*, 17,947-17,963, 1995.

Smith, R.B., and R.L. Bruhn, Intraplate extensional tectonics of the eastern Basin-Range: inferences on structural style from seismic reflection data, regional tectonics, and thermal-mechanical models of brittle-ductile deformation, *J. Geophys. Res., 89*, 5733-5762, 1984.

Walcott, R.I., Flexural rigidity, thickness, and viscosity of the lithosphere, *J. Geophys. Res., 75*, 3941-3954, 1970.

Willet, S.D., D.S. Chapman, and H.J. Neugebauer, A thermo-mechanical model of continental lithosphere, *Nature, 314*, 520-523, 1985.

APPENDIX

Shoreline Elevation Data

	Longitude	Latitude	Elevation	Uncertainty	Method
AI1	-112.1970	40.9279	1602	1	cross-correlation
Will1	-112.0204	41.3821	1575	2	cross-correlation
Oly	-111.8027	40.6509	1591	2	cross-correlation
Og1	-111.9212	41.2335	1588	3	cross-correlation
Og2	-111.9232	41.2309	1582	1	cross-correlation
HV5_1	-111.7305	40.0098	1560	2	cross-correlation
HV3_2	-111.6185	40.2105	1573	5	cross-correlation
Hon3	-112.0519	41.62	1573	2	cross-correlation
Cache1	-111.7938	41.7192	1576	2	cross-correlation
Cache4	-111.7747	41.9788	1563	4	cross-correlation
Magna2	-112.1226	40.6874	1587	5	cross-correlation
Farm1	-111.8840	41.0035	1585	1	cross-correlation
NO1	-111.9365	41.2964	1583	1	cross-correlation
LP2	-112.2483	40.5993	1594	4	cross-correlation
NO2	-111.9405	41.2847	1581	4	cross-correlation
Og1_2	-111.9231	41.2308	1586	3	cross-correlation
Oq1	-112.2409	40.7057	1594	1	cross-correlation
Prom1	-112.4829	41.3113	1605	1	cross-correlation
Prom3	-112.4101	41.2871	1596	2	cross-correlation
Prom4	-112.5077	41.4399	1602	2	cross-correlation
Prom5	-112.6109	41.6064	1597	1	cross-correlation
Franklin	-111.8079	42.0737	1569	3	cross-correlation
Baxter	-111.8871	41.5831	1576	1	Depositional
ESC6_1	-112.9808	38.2999	1554	1	Depositional
ESC1	-113.3389	38.1121	1553	1	Depositional
ESC2_2	-113.2064	38.1437	1554	1	Depositional
ESC2_3	-113.2260	38.1940	1553	1	Depositional
ESC7_2	-113.0801	38.3525	1553	1	Depositional
ESC6_3	-112.9581	38.4673	1553	1	Depositional
ESC8_1	-113.0535	38.4755	1556	1	Depositional
ESC11_2	-112.8644	38.6199	1561	1	Depositional
Mill1_3	-112.6298	38.7692	1577	1	Depositional
Mill1_4	-112.8004	38.8087	1562	1	Depositional
Mill4_2	-113.0052	38.0052	1563	1	Depositional
Mill5_1	-112.3074	39.0463	1559	1	Depositional
Mill3_4	-112.3510	38.9214	1564	1	Depositional
Mill6_1	-112.3209	38.2105	1565	1	Depositional
Mill6_2	-112.3503	39.2392	1565	1	Depositional
Mill7_1	-113.1130	38.6941	1562	1	Depositional
Beav1_1	-113.3051	38.6035	1559	1	Depositional

Beav2_1	-113.3721	38.4223	1555	1	Depositional
Mill10_1	-113.1838	39.2704	1573	1	Depositional
Mill12_2	-113.2013	39.4702	1580	1	Depositional
AI_1Dep	-112.1992	40.9265	1599	1	Depositional
CCDepo	-111.8704	40.7951	1584	1	Depositional